ARHGAP17 regulates the spatiotemporal activity of Cdc42 at invadopodia

Gabriel Kreider-Letterman[1], Abel Castillo[1], Eike K. Mahlandt[2], Joachim Goedhart[2], Agustin Rabino[1], Silvia Goicoechea[1], and Rafael Garcia-Mata[1,*]

[1]Department of Biological Sciences, University of Toledo, Toledo, Ohio, USA

[2]Swammerdam Institute for Life Sciences, Section of Molecular Cytology, van Leeuwenhoek Centre for Advanced Microscopy, University of Amsterdam, Amsterdam, The Netherlands

*Corresponding author: rafael.garciamata@utoledo.edu

Abstract

Cancer cells form actin-rich protrusions called invadopodia that can degrade the extracellular matrix and facilitate tumor invasion and intravasation. Invadopodia formation is regulated by Rho GTPases; however, the molecular mechanisms controlling Rho GTPase signaling at invadopodia are poorly understood. Here, we have identified ARHGAP17, a Cdc42-specific RhoGAP, as a key regulator of invadopodia in breast cancer cells. Using a combination of fixed and live cell imaging, and a Cdc42 sensor optimized for mammalian cells, we have defined a novel ARHGAP17-mediated signaling pathway that controls the spatial and temporal regulation of Cdc42 activity during invadopodia turnover. During assembly, ARHGAP17 localizes to the invadopodia adhesion ring where it restricts the activity of Cdc42 to the invadopodia core. Later, at the start of invadopodia disassembly, ARHGAP17 moves to the core where it inactivates Cdc42 to promote the disassembly of invadopodia in a process that is mediated by its interaction with the Cdc42 effector CIP4. Our results show that ARHGAP17 coordinates when and where Cdc42 is activated during invadopodia assembly and controls the disassembly by terminating the signal.

Introduction

The risks associated with cancer metastasis makes breast cancer one of the leading causes of cancer related mortality among women. One way that metastatic cancer cells invade tissues is through the formation of protrusive, actin-rich structures called invadopodia, which mediate the degradation of the extracellular matrix (ECM) (Murphy and Courtneidge, 2011). The ability of cancer cells to form invadopodia has been correlated with their metastatic potential, and the loss of invadopodia with decreased tumorigenicity and dissemination (Meirson et al., 2018; Stoletov and Lewis, 2015; Yamaguchi, 2012). In addition, studies using intravital microscopy have documented the existence of invadopodia and confirmed their importance for intra/extravasation and dissemination *in vivo* (Gligorijevic et al., 2014).

The structure of invadopodia is typically comprised of an actin-rich core that is surrounded by a ring of adhesion and scaffolding proteins, like that of podosomes which occur in normal cells (Murphy and Courtneidge, 2011). Invadopodia form through a series of steps that is initiated by the disassembly of focal adhesions and stress fibers, and the recycling of many of their components into new invadopodia (Hoshino et al., 2012; Oikawa et al., 2008). Assembly of new invadopodia starts with the formation of actin- and cortactin-rich puncta, closely followed by the recruitment of adhesion proteins such as

vinculin and paxillin (Hoshino et al., 2013). Invadopodia reach maturity upon the recruitment of matrix metalloproteases which facilitate matrix degradation (Hoshino et al., 2013). There is less known about the steps of invadopodia disassembly although the Rho GTPase RhoG and tyrosine phosphorylation of paxillin have been implicated in the process (Badowski et al., 2008; Goicoechea et al., 2017).

The dramatic rearrangement of the actin cytoskeleton during invadopodia formation is regulated by the Rho family of small GTPases (Murphy and Courtneidge, 2011). Rho GTPases function as molecular switches that cycle between an active GTP-bound and an inactive-GDP bound state. The activation of Rho proteins is catalyzed by RhoGEFs (guanine nucleotide exchange factors), whereas RhoGAPs (GTPase-activating proteins) mediate their inactivation. There are 80 RhoGEFs and 66 RhoGAPs in humans, allowing cells to tightly regulate the activity of Rho proteins through multiple pathways (Kreider-Letterman et al., 2022a; Rossman et al., 2005). Since RhoGAPs play a critical role in the termination of signal transduction, mutations in genes encoding RhoGAPs have drastic consequences and underlie several human diseases including cancer (Kreider-Letterman et al., 2022a). RhoGAPs are generally considered tumor suppressors, and the loss of GAP activity results in aberrant GTPase activity which can promote tumorigenesis (Kreider-Letterman et al., 2022a). However, compared with RhoGEFs, which have been studied more extensively, there is significantly less known about RhoGAPs, especially regarding their role in cancer progression and metastasis. The need to better characterize RhoGAPs in cancer progression includes invadopodia as there is increasing evidence that RhoGAPs play a role in their regulation (Al Haddad et al., 2020; Bravo-Cordero et al., 2011; Diring et al., 2019; Nakahara et al., 1998; Noll et al., 2019).

Several Rho proteins are known to be directly involved in invadopodia formation, including Cdc42, Rac1, RhoA, RhoC and RhoG (Ayala et al., 2009; Bravo-Cordero et al., 2011; Goicoechea et al., 2017; Moshfegh et al., 2014; Sakurai-Yageta et al., 2008; Yamaguchi et al., 2005). However, the molecular mechanisms of their spatiotemporal activity at invadopodia, as well as the identity of their upstream regulators and downstream effectors remain poorly characterized. Here, we conducted a candidate shRNA screen to find RhoGAPs involved in invadopodia formation and identified ARHGAP17 (RICH1, Nadrin), a Cdc42-specific GAP and a negative regulator of invadopodia in triple negative breast cancer cells. Using a combination of fixed and live cell imaging and a Cdc42 sensor optimized for mammalian cells, we were able to define a novel signaling pathway involving ARHGAP17, Cdc42, and its effector CIP4 (TRIP10), that controls invadopodia turnover. Our results show that ARHGAP17 is targeted to the ring region of invadopodia during assembly, which functions to restrict the activity of Cdc42 to the core of invadopodia. Upon disassembly, ARHGAP17 is recruited to the invadopodia core by the Cdc42 effector CIP4, where it inactivates Cdc42, and promotes invadopodia disassembly. Altogether, our results identify ARHGAP17 at the center of the dynamic regulation of invadopodia assembly and disassembly and provide new insights on the molecular mechanisms controlling these processes.

Results

ARHGAP17 is a negative regulator of invadopodia in breast cancer cells

To characterize the role of RhoGAPs during invadopodia formation, we used the triple negative breast cancer (TNBC) cell line SUM159 as a model. SUM159 cells produce invadopodia that are highly dynamic and typically form in clusters under the nucleus or as bands at the leading edge (Figure 1A, Figure 1-video 1) (Goicoechea et al., 2017). When grown in culture, the cells form invadopodia clusters

80 spontaneously at low levels (≈1% cells) (Figure 1-figure supplement 2B). However, treatment with the
81 phorbol ester Phorbol 12,13-dibutyrate (PDBu) stimulates the formation of large numbers of
82 invadopodia, with about 30% of cells forming invadopodia after 30 minutes (Figure 1-video 1)
83 (Goicoechea et al., 2009; Goicoechea et al., 2017). To identify RhoGAPs that may regulate invadopodia
84 formation, we performed an shRNA screen on a panel of candidate RhoGAPs in PDBu treated SUM159
85 cells (Figure 1B). We tested 19 RhoGAP candidates using 5 targeting sequences per gene. Several
86 RhoGAPs showed differences in the percentage of cells with invadopodia, typically an increase. Here, we
87 focus on ARHGAP17, as silencing its expression showed the most prominent increases in the percentage
88 of cells forming invadopodia, especially with shRNA sequences #3 and #5. We confirmed the efficiency
89 of the shRNA targeting sequences by western blot analysis, which shows a significant reduction of
90 ARHGAP17 expression in both sequences #3 and #5 when compared to the non-targeting control (Figure
91 1C). We also repeated the invadopodia assay with both shRNA sequences and confirmed that depletion
92 of ARHGAP17 resulted in significant increases in the number of cells that form invadopodia after PDBu
93 treatment (from 28.7% in CTRL cells to 79.3% and 72.3% in shRNAs #3 and #5 respectively) (Figure 1D).
94 We also observed similar results using two unique CRISPR KO sequences for ARHGAP17 (Figure 1-figure
95 supplement 1A and B). In addition, we were able to rescue the effects of silencing ARHGAP17 on
96 invadopodia by re-expressing an shRNA resistant myc-ARHGAP17 (Figures 1E-G). The increase in cells
97 forming invadopodia observed in ARHGAP17 KD was independent of PDBu treatment as silencing
98 ARHGAP17 also induced a significant increase in the number of spontaneous invadopodia in untreated
99 cells (from 1.3% in CTRL cells to 7.8% in ARHGAP17 KO) (Figure 1-figure supplement 2A and B). These
100 results validated the specificity of the phenotype and demonstrated that the results are not dependent
101 on PDBu treatment. Taken together, these results suggest that ARHGAP17 functions as a negative
102 regulator of invadopodia.

103 **ARHGAP17 regulates invadopodia-based matrix degradation and inhibits invasion**

104 To determine whether the increases in invadopodia in the absence of ARHGAP17 resulted in more
105 invadopodia activity, we used a matrix degradation assay in which we plated SUM159 cells on a
106 fluorescent gelatin/collagen IV matrix and treated them with PDBu for 24 hours (Martin et al., 2012).
107 SUM159 cells degraded the matrix with a punctate pattern typical for invadopodia; characterized by F-
108 actin puncta overlapping with a loss of matrix fluorescence, provided the cell had not moved before
109 fixation (Figure 2A) (Artym et al., 2006). We quantified invadopodia activity in CTRL, ARHGAP17 KO, and
110 Rescue cells by measuring the area of degradation/cell area. We found a significant increase in matrix
111 degradation In ARHGAP17 KO cells (≈3-fold) which was rescued to CTRL levels by re-expressing
112 ARHGAP17 (Figure 2B and C). These results demonstrate that invadopodia are still functional in the
113 absence of ARHGAP17.

114 Since silencing the expression of ARHGAP17 results in increased matrix degradation via invadopodia, we
115 would predict the cells to be more invasive when grown in 3D. To determine if ARHGAP17 KD cells are
116 more invasive, we performed a 3D spheroid invasion assay (Vinci et al., 2015). In this assay, SUM159
117 cells were grown in ultra-low attachment plates that resulted in the formation of a spheroid reminiscent
118 of a small tumor (Figure 2D). When the spheroids are embedded in Matrigel, invasive cells migrate away
119 from the spheroid and into the matrix. Spheroid growth and invasion can then be quantified by
120 measuring the area of the spheroid over time. We found that even though ARHGAP17 KD spheroids
121 grew at a slower rate (Figure 2E), they were significantly more invasive when invasion was normalized
122 by average proliferation (Figure 2F). To validate the spheroid invasion results without the effect of

growth impacting the results we also performed an inverse invasion assay. In this assay, we plated SUM159 cells stably expressing mScarlet-CAAX (membrane marker) at the bottom of a plate, overlaid them with a layer of Matrigel and stimulated them to invade upwards by adding serum-containing media on top of the Matrigel (Figure 2G, Figure 2-video 1). Quantification showed that ARHGAP17 KO cells invaded significantly more than the CTRL and that this effect was rescued by re-expressing WT ARHGAP17 (Figure 2H).

ARHGAP17 regulates invadopodia dynamics

The dramatic increase in invadopodia observed in ARHGAP17 KD cells suggested that ARHGAP17 could be modulating invadopodia turnover. Interestingly, in the absence of ARHGAP17, not only were more cells able to form invadopodia compared to CTRL cells, but also the invadopodia clusters were larger (Figure 3A). This may reflect a change in invadopodia dynamics, possibly due to an increase in invadopodia lifetime or defects in disassembly signaling. To further explore this possibility, we performed a time-course experiment in which we treated SUM159 cells (CTRL, ARHGAP17 KD, and Rescue) with PDBu and quantified the percentage of cells forming invadopodia at successive time points after treatment (Figure 3B). As we have previously described (Goicoechea et al., 2017), CTRL cells showed a rapid spike in invadopodia forming cells at the 10-minute mark that then decreased rapidly until reaching equilibrium at 30 minutes, with approximately 30% of cells being positive for invadopodia at any given time afterwards. Interestingly, the initial increase in invadopodia was larger in ARHGAP17 KD cells (>80% positive cells at 10 min), and the decrease not as pronounced, with invadopodia percentages reaching an equilibrium at a much higher percentage (>60% after 30 min). Re-expressing ARHGAP17 restored the normal time-course dynamics (Figure 3B). When we calculated the difference in percentage of cells with invadopodia between the 10- and 30-min time points, i.e., the drop-off from peak to equilibrium, the difference was significantly smaller in ARHGAP17 KD cells when compared to CTRL or Rescue (50% reduction in CTRL vs. 20% reduction in ARHGAP17 KD) (Figure 3-figure supplement 1A). These results suggest that in the absence of ARHGAP17, the invadopodia may be more stable and thus longer lived.

We next wanted to characterize the role of ARHGAP17 on invadopodia dynamics. The dynamics of single invadopodia can be divided into three defined stages: assembly, stability, and disassembly. This is illustrated in Figure 3C, in which the intensity of the invadopodia marker TKS5-mTagBFP2 was measured over the lifetime of a single invadopodia. Using live Total Internal Reflection Fluorescence (TIRF) microscopy and a custom algorithm inspired by a similar method previously used to quantify focal adhesions (Berginski et al., 2011), we were able to accurately measure the dynamics of invadopodia formation after PDBu treatment with high enough resolution to resolve the individual invadopodia from the clusters (Figure 3D). Using this method, we found that individual invadopodia have increased overall lifetime in ARHGAP17 KO cells (Figure 3D and E), and that this increase in lifetime was a result of an increase in the duration of the stability phase (Figure 3H) and not due to significant changes in the duration of the assembly or disassembly phases (Figures 3F and G). In agreement, we found no significant changes in the assembly or disassembly rates (Figure 3-figure supplement 2A and B). We also summarized the results using a Principal Component Analysis (PCA) which shows that ARHGAP17 KO invadopodia form a distinct population on the bases of lifetime and stability with only minimal impact from the other variables (Figure 3-figure supplement 2C). These results demonstrate that ARHGAP17 regulates the dynamics of invadopodia and that, in the absence of ARHGAP17, invadopodia are more stable which is associated with increased accumulation of invadopodia within clusters.

166 **ARHGAP17 is targeted to invadopodia through multiple domains**

167 To visualize the localization of endogenous ARHGAP17 in cells we generated a polyclonal antibody
168 against a small peptide from the C-terminus of ARHGAP17. The antibody recognized a single band by
169 western blot, which disappeared upon KD or KO of ARHGAP17 (Figure 1C, Figure 1-figure supplement
170 1A). In PDBu-treated SUM159 cells, the ARHGAP17 antibody showed a clear signal at the invadopodia
171 clusters. This signal was lost in ARHGAP17 KO cells confirming the specificity of the antibody (Figure 4A).
172 A similar result was observed when expressing an ARHGAP17-GFP construct in ARHGAP17 KO SUM159
173 cells, with ARHGAP17-GFP targeting efficiently to invadopodia as marked by TKS5-mTagBFP2 (Figure 4B).
174 Live imaging analysis showed that ARHGAP17-GFP is recruited early during invadopodia formation,
175 almost simultaneously with Tks5-mTagBFP2, and remains associated until the invadopodia disappears
176 (Figure 4B and Figure 4-video 1). Interestingly, we observed that ARHGAP17 did not perfectly colocalize
177 with TKS5 and had a more diffuse appearance with the signal localized in some cases adjacent to, or in
178 the periphery of TKS5 puncta (Figure 4B, zoom panel).

179 Invadopodia are typically organized with a core region comprised of actin, actin nucleators, and
180 scaffolding proteins, and a surrounding ring comprised of adhesion and adapter proteins such as paxillin
181 or vinculin (Branch et al., 2012). Our initial results suggested that ARHGAP17 may be localized
182 preferentially to the ring region of invadopodia. To better define the localization of ARHGAP17 at
183 invadopodia, we utilized STORM (Stochastic Optical Reconstruction Microscopy) reconstructions of
184 invadopodia using F-actin (phalloidin staining) and cortactin as markers for the invadopodia core, and
185 paxillin as a marker for the ring. We then compared the intensity distribution of these proteins to that of
186 myc-ARHGAP17. We used ARHGAP17 KO SUM159 cells stably expressing myc-ARHGAP17 to facilitate
187 the use of anti-myc antibodies, which provided better results with STORM than staining for the
188 endogenous protein. From these results, ARHGAP17 appears to share its localization pattern more with
189 paxillin than actin or cortactin (Figure 4C, Figure 4-figure supplement 1A and B).

190 To compare the localization of different invadopodia proteins we developed a semi-automatic macro
191 script in ImageJ that measures the intensity of invadopodia proteins in relation to the center of the
192 invadopodia (hereafter referred to as radial intensity analysis). In this script, a line is drawn across the
193 center of each invadopodia. The line is then sequentially rotated 120 times at 3° intervals and the
194 intensity profile is measured at each of the intervals for all fluorescent channels. The mean of all
195 measurements is then used to display the average intensity related to the distance from the center of
196 the invadopodia (Figure 4D). When this method is applied to the STORM reconstructions, we found that
197 ARHGAP17 localization extends further away from the center of the invadopodia when compared to the
198 core proteins cortactin and F-actin, and aligns closely with the ring protein paxillin, suggesting it is a ring
199 protein (Figure 4D). However, unlike paxillin, a fraction of ARHGAP17 is also localized to the core. Figure
200 4D shows that the intensity of myc-ARHGAP17 remains high at the core when compared to that of
201 paxillin, which decreases sharply at the invadopodia center (Figure 4C, Figure 4-figure supplement 1A
202 and B).

203 To determine how ARHGAP17 is targeted to invadopodia, we generated and expressed a series of
204 domain deletion mutants in ARHGAP17 KO SUM159 cells (Figure 5A). Using TIRF microscopy for its high
205 signal-to-noise ratio, we found that both the N-BAR domain and the C-terminus Proline-rich region are
206 important for targeting ARHGAP17 to invadopodia (Figure 5B-E). We then used the radial intensity
207 analysis to precisely define the localization for each of the mutants (Figure 5C). Our results show that

upon deletion of the C-terminus (ΔC), ARHGAP17 localization decreases at the core, but remains associated with the ring, which suggests that the Proline-rich region is important for targeting ARHGAP17 to the center of invadopodia (Figure 5B and C). In this mutant, the ring diameter is also wider (Figure 5D). In contrast, when the N-BAR domain is deleted (ΔBAR), there is an increase in the localization of ARHGAP17 to the core, which is accompanied by a slight reduction in the ring and a more diffuse localization pattern (Figure 5B-D). Interestingly, the N-BAR domain alone is sufficient to target to the core of invadopodia, where it is distributed in a punctate pattern (Figure 5B-E). Deletion of either the C-terminus or the N-BAR domain reduced the total amount of ARHGAP17 recruited to invadopodia compared to the WT protein, which suggests that targeting to invadopodia is partially compromised in both mutants (Figure 5E).

We also tested these deletion mutants for their ability to rescue the ARHGAP17 KO phenotype. Our results show that the ΔC mutant rescues the levels of invadopodia efficiently to a level that is close but still significantly different than that of the WT Rescue. The ΔBAR mutant also showed a reproducible level of rescue although it was less efficient than the ΔC mutant. In contrast, the N-BAR domain alone showed no evidence of rescue, which confirms that the rest of the protein is not only important for targeting but also for ARHGAP17's function. (Figure 5F). From these results, we conclude that ARHGAP17 regulates invadopodia by its ability to associate to both the ring and core structures through the N-BAR domain and C-terminus, respectively.

ARHGAP17 regulation of invadopodia requires its RhoGAP activity for Cdc42

In vitro assays have initially shown ARHGAP17 to have RhoGAP specificity for all three of the ubiquitous Rho GTPases: Cdc42, Rac1, and RhoA (Harada et al., 2000). However, later studies suggest it is specific for Cdc42 and Rac1 *in vitro* with preference for Cdc42 in cells (Richnau and Aspenstrom, 2001; Richnau et al., 2004; Wells et al., 2006). To assess the specificity of endogenous ARHGAP17 in SUM159 cells, we performed a GAP pulldown assay using glutathione S-transferase (GST)-tagged, constitutively active mutants of RhoA, Rac1, and Cdc42 (Figure 6A) (García-Mata et al., 2006). We found that ARHGAP17 precipitated with active Cdc42 but not with RhoA or Rac1. Furthermore, when the expression of ARHGAP17 was silenced in SUM159 cells, there was a significant increase in total Cdc42 activity in the cells as determined by an affinity pulldown assay (Figure 6B). From these results, we determined that ARHGAP17 is specific for Cdc42 in SUM159 cells.

Since Cdc42 signaling is known to be essential for the formation of invadopodia (Ayala et al., 2009; Di Martino et al., 2014; Goicoechea et al., 2014; Sakurai-Yageta et al., 2008; Yamaguchi et al., 2005; Zagryazhskaya-Masson et al., 2020), we performed a time course assay in which we measured Cdc42 activity in SUM159 cells at 10-minute intervals following PDBu treatment (Figures 6C). Our results showed a peak in Cdc42 activity in CTRL cells that roughly correlates with the time course of invadopodia formation (see Figure 3B). ARHGAP17 KD cells also showed an increase in Cdc42 activity at the same time point (20 min). However, the Cdc42 increase was not as prominent as in CTRL cells, likely because the basal activity of Cdc42 is already comparatively higher at time zero in the ARGHAP17 KD cells (Figure 6B and Figure 6-figure supplement 1A, compare the activity between t0 and t20). These results suggest that ARHGAP17 modulates the activity of Cdc42 during the formation of invadopodia.

To test this prediction, we mutated the critical Arginine finger motif in the RhoGAP domain of ARHGAP17 (R288A), which renders it catalytically dead (CD) (Harada et al., 2000). We then quantified both the localization of ARHGAP17 CD to invadopodia and its ability to rescue the ARHGAP17 KO

250 phenotype. Our results demonstrated that the catalytic activity is not required for targeting ARHGAP17
251 to invadopodia, as the CD mutant localization and radial intensity analysis were indistinguishable from
252 that of the WT protein (Figure 6D and E). The distance from the core and the intensity at the
253 invadopodia were also not significantly different between WT and CD ARHGAP17 (Figure 6F and G).
254 However, despite targeting correctly, the CD mutant was unable to rescue the KO phenotype, which
255 suggests the RhoGAP activity is required for ARHGAP17 to regulate invadopodia turnover (Figure 6H).

256 **Spatiotemporal regulation of Cdc42 by ARHGAP17 at invadopodia**

257 Since ARHGAP17 regulation of invadopodia requires its Cdc42-specific RhoGAP activity, we wanted to
258 characterize the spatiotemporal regulation of Cdc42 activity and ARHGAP17 at invadopodia. To monitor
259 the dynamics of Cdc42 activity in live cells, we utilized a localization based Cdc42 biosensor (dTomato-
260 wGBD) consisting of the GTPase-binding domain of the Cdc42 effector WASP (wGBD) linked to the
261 dTomato fluorescent protein (Figure 7A). The wGBD domain will localize to active Cdc42 in the cell but is
262 lacking the domains that bind other proteins such as Cdc42 effector proteins (e.g., CIP4) (Tian et al.,
263 2000). This sensor design has been extensively used in the past, particularly in Xenopus studies, but was
264 typically not sensitive enough for mammalian cell studies (Benink and Bement, 2005; Kim et al., 2000;
265 Vaughan et al., 2011). Our new Cdc42 sensor has been designed using the same iterative approach we
266 recently described for a RhoA sensor (Mahlandt et al., 2021). To verify the specificity of the sensor in
267 SUM159 cells, we used an assay that measures the translocation of the sensor to the nucleus when co-
268 expressed with different nuclear localized constitutively active Rho GTPases as we have previously
269 described (Mahlandt et al., 2021). Our results show that the dTomato-wGBD sensor is highly specific for
270 Cdc42, with only residual binding to Rac1, and no detectable binding to RhoA (Figure 7-figure
271 supplement 1A and B). We then tested the localization of the sensor in SUM159 cells stimulated with
272 PDBu to form invadopodia. Upon treatment of PDBu, the sensor strongly re-localizes to newly forming
273 invadopodia, indicating an increase in Cdc42 activity specifically at invadopodia (Figure 7B, Figure 7-
274 video 1). We also followed the activity of Cdc42 in single invadopodia over time and compared it with
275 the intensity of ARGHAP17-GFP and TKS5-mTagBFP2. We found that the sensor signal follows the
276 progression of the invadopodia, increasing in intensity during its assembly and decreasing as the
277 invadopodia disappears (Figure 7C, Figure 7-video 2). Interestingly, we observed that the appearance of
278 Cdc42 activity is more pronounced at the initial stages of invadopodia formation, while ARHGAP17-GFP
279 appears in the second half of invadopodia assembly with a slight increase in signal as the invadopodia
280 disassemble (Figure 7C, Figure 7-video 2). Quantitative analysis of intensity over time in multiple
281 invadopodia confirmed this observation (Figure 7D). Cross-correlation analysis between TKS5-
282 mTagBFP2, ARHGAP17-GFP, and dTomato-wGBD showed that there is a positive correlation between
283 the three proteins (Figure 7E). The strongest correlation observed was between Cc42 activity and TKS5,
284 with Cdc42 activity occurring slightly earlier in time than TKS5. In contrast, the correlation between
285 ARHGAP17 and either Cdc42 activity or TKS5 was weaker, likely due to the ring localization of
286 ARHGAP17, with ARHGAP17 appearing later than both Cdc42 and TKS5. In addition, we found that in the
287 absence of ARHGAP17 (ARHGAP17 KO) there was a significant increase in the maximum Cdc42 activity at
288 invadopodia when compared to CTRL or ARHGAP17 Rescue cells (Figure 7F).

289 To characterize the spatiotemporal dynamics of ARHGAP17 and Cdc42 throughout the lifecycle of
290 invadopodia, we used the radial intensity analysis method described for single invadopodia in Figure 4
291 for each frame in time-lapse series of single invadopodia co-expressing Tks5-mTagBFP2, ARHGAP17-GFP,
292 and the Cdc42 sensor (as in Figure 7C). A representative kymograph of several invadopodia averaged

293 together is shown, which displays the signal intensity over time (x-axis, normalized to be comparable), as
294 well as the localization of the signal in relation to the center of the invadopodia (y-axis) (Figure 7G).
295 These results showed that Cdc42 activity (wGBD) was tightly localized at invadopodia, specifically at the
296 core throughout the lifetime of invadopodia. During the invadopodia assembly phase, ARHGAP17 is
297 recruited preferentially to the invadopodia ring as expected from our results from fixed images in Figure
298 4. Surprisingly, when the invadopodia starts to disassemble, the localization of ARHGAP17 shifts from
299 the ring to the core, and this shift coincides with a decrease in Cdc42 signal at the core. This change in
300 localization can also be visualized as line profiles of selected time points from the time series data
301 (Figure 7H and I). At an early stage during invadopodia assembly (t 0.25), ARHGAP17 was found
302 predominantly in the ring (Figure 7H), while later during invadopodia disassembly (t 0.75), ARHGAP17
303 was shifted to the core (Figure 7I). This shift of ARHGAP17 to the core is also associated with a decrease
304 in peak TKS5 intensity and an even more severe decrease in peak wGBD intensity (Figure 7H) when
305 compared to assembly (Figure 7I). Taken together, these data suggest that ARHGAP17 at the ring
306 restricts the activity of Cdc42 to the core during invadopodia assembly and moves to the core later,
307 where it inactivates Cdc42 to promote invadopodia disassembly.

308 **An ARHGAP17/CIP4/Cdc42 complex regulates invadopodia**

309 We have shown that ARHGAP17 regulates Cdc42 at invadopodia in a RhoGAP-dependent manner.
310 However, we do not know what Cdc42 effector is downstream of this signaling pathway. A potential
311 candidate is Cdc42-interacting protein 4 (CIP4), a Cdc42 effector which has been previously shown to
312 interact with ARHGAP17 (Richnau and Aspenstrom, 2001). Furthermore, CIP4 also targets to
313 invadopodia and regulates their formation in breast cancer cells (Pichot et al., 2010). To validate these
314 observations in our model, we generated SUM159 cells stably expressing shRNA for CIP4 (Figure 8A) and
315 found that, as described previously (Pichot et al., 2010), there was a significant decrease in the
316 percentage of cells forming invadopodia when the expression of CIP4 was silenced (Figure 8B and C). We
317 then stained for endogenous CIP4 in PDBu-treated SUM159 cells and confirmed that CIP4 also targets
318 specifically to invadopodia in these cells (Figure 8D) and localizes predominantly to the invadopodia core
319 (Figure 8E). We also confirmed that ARHGAP17 binds CIP4 at endogenous levels using co-
320 immunoprecipitation (Figure 8F) and that the proline-rich region of ARHGAP17 is required for CIP4
321 binding as was previously shown (Figure 8G) (Richnau and Aspenstrom, 2001). We next wanted to
322 determine if ARHGAP17 activity is coupled with CIP4 as part of a complex to regulate Cdc42 activity as
323 has been frequently observed with RhoGEFs and some RhoGAPs (Lawson and Ridley, 2018). Using GST-
324 Cdc42 Q61L and CD ARHGAP17-GFP (which does not interact with Cdc42), we found that myc-CIP4 can
325 bind to active Cdc42 and CD ARHGAP17-GFP simultaneously (Figure 8G), suggesting that they may form
326 a complex in cells.

327 We then wanted to characterize the roles of the ARHGAP17, CIP4, and Cdc42 activity in invadopodia.
328 When analyzing individual invadopodia expressing CIP4-GFP, TKS5-mTagBFP2, and dTomato-wGBD, we
329 found that CIP4 is present at invadopodia throughout their lifetime and corresponds closely with TKS5,
330 both spatially and temporally (Figure 9A and B). Interestingly, Cdc42 activity, as determined by the
331 dTomato-wGBD biosensor, was present earlier in invadopodia lifetime than CIP4, while CIP4 was still
332 present in invadopodia after loss of Cdc42 activity (Figure 9A and B). These temporal shifts between
333 CIP4 and Cdc42 activity were confirmed using cross-correlation analysis (Figure 9C). To determine the
334 role of the ARHGAP17-CIP4 interaction in the regulation of invadopodia, we investigated the localization
335 of ARHGAP17 (ARHGAP17-GFP expressed in ARHGAP17 KO cells) in CTRL cells compared to cells

336 overexpressing myc-CIP4. Interestingly, in cells overexpressing myc-CIP4, we observed a dramatic shift
337 from the typical ARHGAP17 localization enriched at the ring, to a predominantly core localization (Figure
338 9D and E; top and middle panels). This was dependent on the interaction between ARHGAP17 and CIP4
339 since the ΔC ARHGAP17-GFP mutant, which does not interact with CIP4, failed to relocate to the core
340 when co-expressed with myc-CIP4 (Figure 9D and E; bottom panels). Cross-correlation analysis of
341 invadopodia clusters confirmed these results, with a high cross-correlation coefficient between
342 ARHGAP17-GFP and myc-CIP4, which decreased drastically for the ΔC ARHGAP17-GFP and myc-CIP4 pair
343 (Figure 9F), even though both proteins still localized to invadopodia (Figure 9D; bottom panels). These
344 results suggest that the translocation of ARHGAP17 from the ring to the core observed upon initiation of
345 invadopodia disassembly depends on ARHGAP17's ability to bind to the core localized cdc42 effector
346 CIP4.

347 Finally, we wanted to determine how the expression levels of ARHGAP17 and CIP4 influence each other
348 to regulate the invadopodia phenotype in SUM159 cells. To do this, we either silenced and/or
349 overexpressed CIP4 and ARHGAP17 in all combinations and quantified the percentage of cells forming
350 invadopodia after PDBu treatment. In agreement with what has been shown so far, our results showed
351 that ARHGAP17 and CIP4 have antagonistic roles at invadopodia. CIP4 overexpression increased the
352 number of cells with invadopodia while ARHGAP17 overexpression had an inhibitory effect. The
353 opposite is true for silencing their expression, with ARHGAP17 KO increasing and CIP4 KD decreasing the
354 number of cells with invadopodia (as shown in previous figures). When we tested combinations of
355 overexpressing and silencing ARHGAP17/CIP4, the function of one protein either synergized or
356 counteracted the effect of the other depending on the combination. If the two proteins were
357 simultaneously overexpressed or silenced, the phenotypic effects balanced each other out. For example,
358 the increase in invadopodia induced by CIP4 overexpression is restored to CTRL levels when ARHGAP17
359 is co-expressed. In contrast, a combination of silencing one gene and overexpressing the other worked
360 to exacerbate the phenotype. For example, ARHGAP17 KO with CIP4 overexpression showed higher
361 levels of invadopodia than either ARHGAP17 KO or CIP4-GFP overexpression alone (Figure 9G). Taken
362 together, our results suggest that the expression levels of ARHGAP17 and CIP4 help regulate the
363 equilibrium between invadopodia assembly and disassembly.

364 Discussion

365 Here, we have identified a novel role for ARHGAP17 in TNBC invadopodia dynamics by restricting the
366 activity of Cdc42 in time and space during invadopodia turnover. Our results demonstrate that the
367 function of ARHGAP17 is important throughout the invadopodia lifecycle. At early stages, during
368 invadopodia growth, ARHGAP17 localizes to the invadopodia ring, which helps to limit the activity of
369 Cdc42 to the actin core. Later, when invadopodia begin to disassemble, ARHGAP17 relocates to the
370 core, where it inactivates Cdc42 and promotes the disassembly of invadopodia (Figure 10). It should be
371 noted that, even in ARHGAP17 KO cells, invadopodia are still able to disassemble. This could be
372 indicative of redundancy in the system. ARHGAP17 has two closely related members of the RhoGAP
373 family, ARHGAP44 (RICH2) and SH3BP1, which may be compensating for the loss of ARHGAP17
374 (Aspenstrom, 2018). Both SH3BP1 and ARHGAP44 have been associated with migration and invasion in
375 cancer cells but have not yet been studied in invadopodia (Parrini et al., 2011; Wang et al., 2018; Zhang
376 et al., 2019). It is likely that one or both proteins regulate invadopodia and would be attractive subjects
377 for future studies.

Our report is the first to describe ARHGAP17 at invadopodia and a direct mechanism regarding the link between ARHGAP17 and cancer cell invasion. ARHGAP17 has been previously characterized as a tumor suppressor and found to be downregulated in a variety of cancers, including colon, breast and cervical, where it functions to inhibit migration and invasion (Guo et al., 2019; Kiso et al., 2018; Pan et al., 2018; Pan et al., 2022; Tian et al., 2022). ARHGAP17 is downregulated by VEGF/NRP1 signaling in TNBC which was associated with increased Cdc42 activity, filopodia formation, and cell migration (Kiso et al., 2018). ARHGAP17 expression was also found to inhibit invasion and metastasis of colon cancer in association with decreased Wnt signaling (Pan et al., 2018), and in cervical cancer, ARHGAP17 suppressed cell proliferation and tumor growth by inhibiting PI3K/AKT signaling (Guo et al., 2019). Our results suggest that the tumor suppressor role of ARHGAP17 may depend in part in its ability to negatively regulate invadopodia by inactivating Cdc42, leading to a decreased invasive capacity.

Cdc42 activity has long been recognized to be essential for both invadopodia and podosome formation, regardless of the cell type or model system used (Ayala et al., 2009; Di Martino et al., 2014; Juin et al., 2014; Moreau et al., 2003; Yamaguchi et al., 2005). Using our improved localization-based sensor, we found that Cdc42 activity is present throughout the lifetime of invadopodia at the invadopodia core with the strongest activity being present at the assembly phase and a decrease in activity being associated with invadopodia disassembly. Cdc42 promotes the assembly of the actin core of invadopodia through its effector N-WASP, which induces actin nucleating by activation of the Arp2/3 complex (Desmarais et al., 2009; Juin et al., 2012; Juin et al., 2014; Lorenz et al., 2004; Monteiro et al., 2013; Yamaguchi et al., 2005; Yu et al., 2012). N-WASP also binds to the SH3 domain of the invadopodia protein, TKS5 (Oikawa et al., 2008). The link between Cdc42 and TKS5 is critical as Cdc42 activity and TKS5 are both essential for invadopodia formation and function (Di Martino et al., 2014). Cdc42 activity also promotes invadopodia function as marked by matrix degradation. Together with RhoA activity, Cdc42 has been shown to promote ECM degradation through its interaction with the Cdc42 effector, IQGAP (Sakurai-Yageta et al., 2008). Interactions between IQGAP and the exocyst protein complex control the delivery of matrix metalloproteases to the membrane of invadopodia (Sakurai-Yageta et al., 2008). Inactivation of Cdc42 at invadopodia by ARHGAP17 would then lead to the reduction of invadopodia formation and activity by shutting down Cdc42-mediated actin nucleation and metalloprotease transport.

The activity of several Rho GTPases has been associated with invadopodia formation and activity, but very few have been studied at the level of detail shown in this manuscript. An exception is RhoC, which in contrast to what we observed for Cdc42, is active at the ring and inactive at the core. This is regulated by the combined action of the ring-localized p190 RhoGEF and the core localized p190 RhoGAP (Bravo-Cordero et al., 2011). Whether p190RhoGAP shifts from the core-to-the ring to inactivate at RhoC is not clear from this study. However, like our study, it highlights the tight spatial and temporal regulation of Rho GTPases, even within invadopodia subdomains.

We have not characterized the RhoGEF responsible for the activation of Cdc42 in our system. A potential candidate is FGD1, which has been identified in previous reports as the RhoGEF that mediates the activation of Cdc42 at both podosomes and invadopodia (Ayala et al., 2009; Daubon et al., 2011; Zagryazhskaya-Masson et al., 2020). FGD1 localizes to invadopodia in metastatic melanoma and breast cancer cells through its interaction with TKS5 and promotes the assembly of the actin core in a Cdc42-dependent manner (Ayala et al., 2009; Zagryazhskaya-Masson et al., 2020). Another potential RhoGEF candidate is Vav1, which has also been found to play a role in invadopodia formation in pancreatic cancer cells by activating Cdc42 (Razidlo et al., 2014). In future studies, it will be interesting to

421 characterize the RhoGEF in the ARHGAP17/Cdc42/CIP4 pathway and the interplay between GEF and
422 GAP activity in regulating invadopodia dynamics.

423 Our study also shows that the Cdc42 effector CIP4 is important for the spatiotemporal regulation of
424 ARHGAP17 at invadopodia. We found that CIP4 localizes specifically to the invadopodia core, and that its
425 interaction with ARHGAP17 is required for the ring-to-core translocation observed for ARHGAP17 at the
426 initiation of invadopodia disassembly. CIP4 has previously been found to localize at invadopodia and
427 function as a positive regulator of invadopodia formation through activation of N-WASP (Pichot et al.,
428 2010). CIP4 seems to function as a scaffolding platform, as it can interact with Cdc42, N-WASP, Src, and
429 ARHGAP17 (Pichot et al., 2010; Richnau and Aspenstrom, 2001). CIP4 has two closely related family
430 members which have also been shown to localize to invadopodia and promote their formation: FBP17
431 (Formin Binding Protein 17) and Toca-1 (transducer of Cdc42-dependent actin activity) (Chander et al.,
432 2013; Suman et al., 2018; Yamamoto et al., 2011). FBP17 and Toca-1 both interact with Cdc42 and N-
433 WASP, promote the activation of N-WASP, and stimulate actin nucleation through the Arp2/3 complex.
434 (Bu et al., 2010; Ho et al., 2004; Hu et al., 2011; Takano et al., 2008; Tsujita et al., 2013; Tsujita et al.,
435 2006). Considering that silencing CIP4 expression does not completely abolish invadopodia formation,
436 FBP17 and/or Toca-1 may compensate for CIP4 loss in SUM159 cells.

437 CIP4, FBP17, and Toca-1 all can activate N-WASP and have been shown to link its activity to membrane
438 curvature sensing, membrane remodeling, and endocytosis through the F-BAR domains. (Chan Wah Hak
439 et al., 2018; Hartig et al., 2009; Takano et al., 2008; Tsujita et al., 2006). It is possible that CIP4 regulates
440 membrane curvature sensing and/or endocytosis at invadopodia, connecting these processes to actin
441 polymerization through N-WASP activation. Interestingly, ARHGAP17 also encodes a BAR domain at the
442 N-terminus, which is important for its targeting at invadopodia and may also play a role in curvature
443 sensing and membrane remodeling/trafficking. What the functional connection between the BAR
444 domains in CIP4 and ARHGAP17 remains to be determined.

445 It is not clear how the ring-to-core translocation is regulated, but phosphorylation is a possibility. Nagy
446 and colleagues have shown that ARHGAP17 is phosphorylated by PKA/PKG at S702, and that this
447 phosphorylation inhibits its binding to CIP4 (Nagy et al., 2015). It is possible then, that when targeted to
448 the ring, ARHGAP17 is phosphorylated, and an unknown stimulus triggers its dephosphorylation at the
449 initiation of disassembly, allowing it to bind to CIP4 and promoting the translocation to the core and
450 subsequent inactivation of Cdc42. Interestingly, CIP4 is also phosphorylated by PKA at T225, and this
451 phosphorylation appears to promote the formation of invadopodia and enhance its interaction with
452 Cdc42 (Tonucci et al., 2019). Future work will shed light in the exact molecular mechanisms controlling
453 the dynamics of ARHGAP17, Cdc42 and CIP4 in the formation of invadopodia, the role of the activators
454 (RhoGEFs), and their effect on actin polymerization and other cellular functions.

455 Materials and Methods

456 Cell lines

457 HEK 293FT cells (Thermo Fisher Scientific) were used for all the pulldown experiments unless indicated
458 otherwise. The SUM159 cells were a gift from Carol Otey (UNC-Chapel Hill, NC). The HEK 293FT cells
459 were cultured in Dulbecco's modified Eagle's medium (DMEM) (GIBCO) containing 10% fetal bovine
460 serum (FBS) (Sigma-Aldrich), and antibiotics (penicillin-streptomycin) (Corning). The SUM159 cells were
461 cultured in Ham's F12 (Cytiva) with 10% FBS, 5 µg/ml insulin (GIBCO), 1 µg/ml hydrocortisone (Sigma-

462 Aldrich), and antibiotics. All cell lines were grown at 37 °C and 5% CO^2. Mycoplasma was tested regularly
463 by staining with Hoechst 33342 (AnaSpec Inc.).

464 **Reagents and antibodies**

465 Antibodies against the following proteins were used: ARHGAP17 (Custom antibody, antigen sequence:
466 EPHRSIFPEMHSDSASKDVPGR, Pacific Immunology); cortactin (sc-11408) (Santa Cruz); myc (13-2500)
467 (Invitrogen); tubulin (T9028) and vinculin (V9131) (Sigma-Aldrich); CIP4 (612556), paxillin (610051),
468 Cdc42 (610929), and Rac1 (610650) (BD Biosciences). F-actin was stained with Alexa Fluor-405, -488, -
469 594, -647, and -750 conjugated to phalloidin (Thermo Fisher Scientific). For immunofluorescence, the
470 following secondary antibodies were used: Alexa Fluor-488, -568, -594, -647-conjugated anti-mouse-IgG
471 and anti-rabbit-IgG secondary antibodies (A32723, A32731, A11004, A11011, A11032, A11037, A21236,
472 A21245; Thermo Fisher Scientific). For western blot analysis the following secondary antibodies were
473 used: horseradish peroxidase (HRP)conjugated anti-mouse-IgG and anti-rabbit-IgG (715-035-151 and
474 711-035-152; Jackson Immunoresearch). Phorbol-12,13-dibutyrate (PDBu) (P1269) was from Sigma-
475 Aldrich.

476 **DNA constructs**

477 Constructs generated for this study: pCMV-myc-ARHGAP17, pLenti-myc-ARHGAP17, pCI-CD-ARHGAP17-
478 GFP, CMVdel-dTomato-1x-wGBD, pEGFP-ΔBAR-ARHGAP17, pLenti-BAR-ARHGAP17-GFP, pLenti-ΔC-
479 ARHGAP17-GFP, pDG462-ARHGAP17-KO were generated using the pDG462 backbone (Adikusuma et al.,
480 2017) (exon 1 targets: CAGCTGGCTAACCAGACCG and GTTGAACTGCTTCTTCATGG; exon 3 targets:
481 AGCATGGCACCGATGCCGAG and CCAAGCGCTTATGGGAATGG).

482 Previously published or purchased constructs: H2A-mTq2, H2A-mTq2-RhoA-G14V- ΔCAAX, H2A-mTq2-
483 Rac1-G12V-ΔCAAX, H2A-mTq2-Cdc42-G12V- ΔCAAX (Mahlandt et al., 2021); pCMV6-myc-Trip10
484 (OriGene-MR208703); All shRNA were from the RNAi Consortium shRNA Library, purchased through
485 Sigma-Aldrich (Table 1).

486 Constructs received as a gift: pCI-C-EGFP-Rich1 and pCI-C-EGFP-CIP4 (Harvey T. McMahon, MRC
487 Laboratory of Molecular biology); pLV-mNeonGreen-CAAX and pLV-Scarlet-CAAX (Jaap van Buul,
488 Sanquin); pmTagBFP2-N1-TKS5 and pmScarlet-N1-TKS5 (Lou Hodgson, Albert Einstein College of
489 Medicine); pDG462 (Paul Thomas, Addgene plasmid # 100903).

490 **Table 1. shRNAs used in this study**

#	Protein Name	Gene Symbol	Reference Sequence	OligoID-1	OligoID-2	OligoID-3	OligoID-4	OligoID-5
1	CDGAP	CDGAP	NM_020754	TRCN0000047638	TRCN0000047639	TRCN0000047640	TRCN0000047641	TRCN0000047642
2	Chimerin1	CHN1	NM_001025201	TRCN0000047798	TRCN0000047799	TRCN0000047800	TRCN0000047801	TRCN0000047802
3	Chimerin2	CHN2	NM_001039936	TRCN0000047738	TRCN0000047739	TRCN0000047740	TRCN0000047741	TRCN0000047742
4	CIP4	TRIP10	NM_001288962.2	TRCN0000063184	TRCN0000063185	TRCN0000063186	TRCN0000063187	NA
5	DLC-1	DLC1	NM_001164271	TRCN0000047823	TRCN0000047824	TRCN0000047825	TRCN0000047826	TRCN0000047827
6	FilGAP	ARHGAP24	NM_001025616	TRCN0000048303	TRCN0000048304	TRCN0000048305	TRCN0000048306	TRCN0000048307

7	GMIP	GMIP	NM_016573	TRCN0000007093	TRCN0000007094	TRCN0000007095	TRCN0000007096	NA
8	GRAF1	GRAF	NM_001135608	TRCN0000029754	TRCN0000029755	TRCN0000029756	TRCN0000029757	TRCN0000029758
9	GRAF2	ARHGAP10	NM_024605	TRCN0000048473	TRCN0000048474	TRCN0000048475	TRCN0000048476	TRCN0000048477
10	GRIT	RICS	NM_001142685	TRCN0000048358	TRCN0000048359	TRCN0000048360	TRCN0000048361	TRCN0000048362
11	Myosin-IXB	MYO9B	NM_001130065	TRCN0000007137	TRCN0000007138	TRCN0000007139	TRCN0000007140	TRCN0000007141
12	Non-targeting	Non-targeting	NA	RHS4459	NA	NA	NA	NA
13	p190-A	GRLF1	NM_004491	TRCN0000022184	TRCN0000022185	TRCN0000022186	TRCN0000022187	TRCN0000022188
14	p190-B	ARHGAP5	NM_001030055	TRCN0000006475	TRCN0000006476	TRCN0000006477	TRCN0000006479	TRCN0000012703
15	RhoGAP1	ARHGAP1	NM_004308	TRCN0000047298	TRCN0000047299	TRCN0000047300	TRCN0000047301	TRCN0000047302
16	RhoGAP12	ARHGAP12	NM_018287	TRCN0000047263	TRCN0000047264	TRCN0000047265	TRCN0000047266	TRCN0000047267
17	RICH1	ARHGAP17	NM_001006634	TRCN0000047448	TRCN0000047449	TRCN0000047450	TRCN0000047451	TRCN0000047452
18	SRGAP1	SRGAP1	NM_020762	TRCN0000047553	TRCN0000047554	TRCN0000047555	TRCN0000047556	TRCN0000047557
19	SRGAP2	SRGAP2	NM_001042758	TRCN0000047958	TRCN0000047959	TRCN0000047960	TRCN0000047962	TRCN0000166364
20	SRGAP3	SRGAP3	NM_001033117	TRCN0000047563	TRCN0000047564	TRCN0000047565	TRCN0000047566	TRCN0000047567
21	TCGAP	SNX26	NM_001172630	TRCN0000151287	TRCN0000152300	TRCN0000153966	TRCN0000154588	TRCN0000156215

Cell lysis and immunoblotting

Cells cultured on 100 mm tissue culture dishes were rinsed with TBS and 1 mM $MgCl_2$ and then scraped into a lysis buffer containing 50 mM Tris-HCl pH 7.4, 10 mM MgCl2, 150 mM NaCl, 1% Triton X-100, and EZBlock protease inhibitor cocktail (BioVision). The supernatant was collected after centrifugation at 16,800g for 10 min. For immunoblotting, lysates were boiled in 2× Laemmli buffer, and were resolved by SDS-PAGE. The proteins were transferred onto PVDF and immunoblotted with the indicated antibodies. Immunocomplexes were visualized using the Immobilon Western Millipore Chemiluminescence HRP substrate (Millipore).

Rho GTPase activity assay

Active Cdc42 pulldown experiments were performed as described previously (Goicoechea et al., 2014). Briefly, SUM159 cells were lysed in 50 mM Tris-HCl pH 7.4, 10 mM MgCl2, 150 mM NaCl, 1% Triton X-100, and EZBlock protease inhibitor cocktail. After clearing the lysates by centrifugation at 14,000 g for 5 min, the protein concentrations of the supernatants were determined, and equal amounts of total protein were incubated with 50 µg of GST–PBD, and rotated for 30 min at 4 °C. Subsequently the beads were washed three times in lysis buffer. Pull-downs and lysates were then immunoblotted for Cdc42.

Immunofluorescence

508 For TIRF experiments, cells were grown in 8-well 1.5 glass bottom µ-slides (Ibidi), otherwise, cells were
509 grown on 1.5 glass coverslips (Thermo Fisher Scientific). For immunofluorescence, cells were fixed for 10
510 min with 4% paraformaldehyde and quenched with 10 mM ammonium chloride. Cells were then
511 permeabilized with 0.1% Triton X-100 in PBS for 7 min. The coverslips were then washed with PBS and
512 blocked with PBS/2.5% goat serum/0.2% Tween 20 for 5 min, followed by 5 min of blocking with
513 PBS/0.4% fish skin gelatin/0.2% Tween 20. Cells then were incubated with the primary antibody for 1 h
514 at room temperature. Coverslips were washed 5 times with PBS/0.2% Tween 20 followed by 5 min of
515 blocking with PBS/0.4% fish skin gelatin/0.2% Tween 20 and 5 min with PBS/2.5% goat serum/0.2%
516 Tween 20. Secondary antibody diluted in the blocking solution was then added for 45 min, washed 5
517 times with PBS/0.2% Tween, and mounted on glass slides in Mowiol mounting solution (Electron
518 Microscopy Sciences). For TIRF experiments, the cells were washed twice with PBS to remove any
519 detergent and kept in PBS for imaging.

520 **STORM microscopy**

521 For the STORM immunofluorescence, cells were fixed for 10 min with 4% paraformaldehyde and
522 quenched with 10 mM ammonium chloride in 35 mm glass-bottomed dishes (81158, Ibidi). Cells were
523 then permeabilized with 0.1% Triton X-100 in PBS for 7 min. The samples were then washed with PBS
524 and blocked with PBS/2.5% goat serum/0.2% Tween 20 for 10 min, followed by 10 min of blocking with
525 PBS/0.4% fish skin gelatin/0.2% Tween 20. Cells then were incubated with the primary antibody for 1 h
526 at room temperature. Samples were washed 5 times with PBS/0.2% Tween 20 (2 times for 5 min and 3
527 times for 10 min) followed by 10 min of blocking with PBS/0.4% fish skin gelatin/0.2% Tween 20 and 10
528 min with PBS/2.5% goat serum/0.2% Tween 20. Secondary antibody (Alexa Fluor 488 and 647) diluted in
529 the blocking solution was then added for 45 min, washed 5 times with PBS/0.2% Tween as before, and
530 then washed twice with PBS to remove any detergent. Samples were imaged in OxEA buffer (Nahidiazar
531 et al., 2016) for 10,000 frames at 100 Hz for each channel starting with the longer wavelength
532 fluorophore first. The minimal light intensity to sufficiently send the fluorophores to the dark state was
533 used to limit bleaching (Diekmann et al., 2020). Reconstruction of STORM data was performed using
534 Nikon NIS-Elements AR software.

535 **Microscopes**

536 For STORM, TIRF, and live imaging experiments, a Nikon Eclipse Ti2 microscope was used equipped with
537 a Tokai Hit STX stage top incubator, Apo TIRF 60x NA 1.49 oil immersion and SR HP Apo TIRF 100x NA
538 1.49 oil immersion objectives, Hamamatsu ORCA-Flash 4.0 camera, Princeton Instruments ProEM back-
539 illuminated EMCCD camera, Lumencor SPECTRA X solid-state light source, Agilent laser unit (405-, 488-,
540 561-, and 647-nm), and NIS-Elements AR software.

541 Confocal data was collected using a Leica Stellaris 5 laser scanning confocal equipped with an HC PL APO
542 63x/1.40 OIL CS2 objective and LAS X software, or an Andor Dragonfly 200 spinning disk confocal on a
543 Leica DMI8 platform equipped with an HC PL FLUOTAR L 20X air objective, HC PL APO 63x/1.40 oil
544 objective, Zyla4 camera, and Fusion software.

545 Brightfield images were acquired on an Olympus IX81 inverted microscope equipped with a UPlanFL N
546 10×/0.30 Ph1 air objective, Hamamatsu ORCA-Flash 4.0 camera, and cellSens software.

547 **Matrix degradation assay**

548 The matrix degradation assay was modified from the Weed lab protocol (Martin et al., 2012). In brief,
549 glass coverslips were coated with polylysine (50 µg/mL in water) and incubated for 20 minutes at room
550 temperature and washed 3x with PBS. The coverslips were then fixed with ice-cold 0.5% glutaraldehyde
551 in PBS and incubated on ice for 15 minutes and washed 3x with ice-cold PBS. The last wash was
552 completely removed, and the coverslips were coated with a 37 °C solution consisting of 6 parts 1%
553 (w/w) stock gelatin/sucrose solution in PBS, 1 part of Oregon Green 488-conjugated gelatin (Thermo
554 Fisher Scientific), and 2 parts collagen IV (500 µg/mL stock). The excess matrix solution was aspirated off
555 and incubated for 10 min at room temperature in the dark. The coverslips were then washed 3x with
556 PBS and quenched with NaBH4 (5 mg/ml in PBS) for 15 min. The coverslips were washed 3x with PBS
557 and sterilized with 70% ethanol for 30 min at room temperature. Finally, the coverslips were washed 3x
558 with sterile PBS and stored at 4 °C for up to two weeks before use.

559 For the assay, SUM159 cells were plated on the gelatin coverslips and treated with PDBu for 24 hours.
560 The coverslips were then fixed, stained with AlexaFluor-594 Phalloidin, and mounted using the
561 described immunofluorescence protocol. For each condition, 20 random fields-of-view (FOV) were
562 acquired via spinning disk confocal. Degradation was quantified by dividing the area of degradation for
563 each image by the total cell area and normalizing the results to the CTRL cells.

564 **Invasion assays**

565 The spheroid invasion assay was performed using the previously described method (Vinci et al., 2015). In
566 brief, 4,000 cells were transferred into ultra-low attachment (ULA) 96-well round bottom plate in 200 µL
567 of media and grown for 4 days. Once the spheroids had matured, 100 µL of media was removed and 100
568 µL of Matrigel (354230, Corning) was added and allowed to polymerase at 37 °C for 1 hr. After
569 polymerization, 100 µL of media were added on top of the Matrigel. The spheroids were imaged every
570 24 hr for 72 hr. For measuring spheroid proliferation, the same process was followed except the
571 Matrigel was omitted.

572 The inverse invasion assay was modified from previous methods (Goswami et al., 2005; Scott et al.,
573 2011). SUM159 cells stably expressing mNeon-CAAX were plated in a CELLview glass bottom 10-well
574 slide (Greiner Bio-One) to achieve 100% confluency overnight. The cells were then washed 3 times with
575 PBS to remove growth factors and media. 100 µL of 50% Matrigel in serum free media was added to
576 each of the wells. The cells were then incubated at 37 °C for 30 min to polymerize the matrix. 100 µL
577 serum containing media was added to each well. The cells were then incubated overnight and at least 3
578 random regions per well were imaged with spinning disk confocal equipped with a long working distance
579 20X objective.

580 **Radial intensity analysis**

581 Invadopodia radial intensity measurements were performed in ImageJ using a custom macro and the
582 calculations were performed with RStudio. Briefly, a 3 µm line ROI was drawn across the center of a
583 single invadopodia based on the F-actin channel. Then the pixel intensity was measured across the ROI
584 after which the ROI was rotated 3 degrees. This was repeated until the ROI completed a complete
585 revolution and was then repeated for each channel of the image. For each invadopodia measured, the
586 intensity values were averaged together to calculate the average intensity radiating out from the center
587 of the invadopodia. The intensity measurements can then be plotted directly or used to calculate the
588 distance of the peak signal from the center of each invadopodia or the relative signal intensity for each

589 invadopodia by dividing the average signal intensity within 1 µm from the center of the invadopodia by
590 the signal 1.5 µm from the invadopodia center.

591 **Invadopodia dynamics analysis**

592 The invadopodia dynamics measurements were performed in ImageJ using a custom macro and the
593 calculations were performed with RStudio. Briefly, the center of a random, single invadopodia that
594 forms and disassembles within the duration of the video was identified for each frame. Then, for each
595 frame, a 1 µm diameter circle was drawn around the invadopodia and a 1 µm band was drawn around
596 the circle. The average intensity within the circle was then divided by the average intensity within the
597 band to calculate the relative signal intensity at the invadopodia for each frame. The quantification of
598 the dynamics was performed as previously described for cell ruffle dynamics (Kreider-Letterman et al.,
599 2022b).

600 **Statistical analysis**

601 Values calculated from at least three independent experiments were compared by an unpaired
602 student's t-test using GraphPad Prism or RStudio unless otherwise indicated. Otherwise, a one-way
603 ANOVA analysis followed by a Tukey's test was performed. Technical replicates are defined in this study
604 as individual cells or invadopodia while biological replicates are defined as the averages of technical
605 replicates or cell populations from independently prepared samples. Biological replicates were assumed
606 to have normal distribution (Fay and Gerow, 2013). $P<0.05$ was considered statistically significant. Error
607 bars represent the S.E.M. unless otherwise indicated.

608 Acknowledgements

609 The authors would like to thank Carol Otey, Harvey T. McMahon, Jaap van Buul, and Lou Hodgson for
610 providing reagents. This work was supported by a Nederlandse Organisatie voor Wetenschappelijk
611 Onderzoek ALW-OPEN grant (ALWOP.306) (to E.K.M.) and 1R15CA199101, R03CA234693, and R01-
612 GM136826-01 grants from the NIH (to R.G.-M.).

613 Competing interests

614 The authors declare no competing interests.

615 Data availability

616 All datasets generated from this study will be made publicly available.

617 References

618 Adikusuma, F., C. Pfitzner, and P.Q. Thomas. 2017. Versatile single-step-assembly CRISPR/Cas9 vectors
619 for dual gRNA expression. *PLoS One*. 12:e0187236.
620 Al Haddad, M., R. El-Rif, S. Hanna, L. Jaafar, R. Dennaoui, S. Abdellatef, V. Miskolci, D. Cox, L. Hodgson,
621 and M. El-Sibai. 2020. Differential regulation of rho GTPases during lung adenocarcinoma
622 migration and invasion reveals a novel role of the tumor suppressor StarD13 in invadopodia
623 regulation. *Cell Commun Signal*. 18:144.

624 Artym, V.V., Y. Zhang, F. Seillier-Moiseiwitsch, K.M. Yamada, and S.C. Mueller. 2006. Dynamic
625 interactions of cortactin and membrane type 1 matrix metalloproteinase at invadopodia:
626 defining the stages of invadopodia formation and function. *Cancer Res*. 66:3034-3043.
627 Aspenstrom, P. 2018. BAR Domain Proteins Regulate Rho GTPase Signaling. *Adv Exp Med Biol*.
628 Ayala, I., G. Giacchetti, G. Caldieri, F. Attanasio, S. Mariggio, S. Tete, R. Polishchuk, V. Castronovo, and R.
629 Buccione. 2009. Faciogenital dysplasia protein Fgd1 regulates invadopodia biogenesis and
630 extracellular matrix degradation and is up-regulated in prostate and breast cancer. *Cancer Res*.
631 69:747-752.
632 Badowski, C., G. Pawlak, A. Grichine, A. Chabadel, C. Oddou, P. Jurdic, M. Pfaff, C. Albigès-Rizo, and M.R.
633 Block. 2008. Paxillin phosphorylation controls invadopodia/podosomes spatiotemporal
634 organization. *Mol Biol Cell*. 19:633-645.
635 Benink, H.A., and W.M. Bement. 2005. Concentric zones of active RhoA and Cdc42 around single cell
636 wounds. *J Cell Biol*. 168:429-439.
637 Berginski, M.E., E.A. Vitriol, K.M. Hahn, and S.M. Gomez. 2011. High-resolution quantification of focal
638 adhesion spatiotemporal dynamics in living cells. *PLoS One*. 6:e22025.
639 Branch, K.M., D. Hoshino, and A.M. Weaver. 2012. Adhesion rings surround invadopodia and promote
640 maturation. *Biol Open*. 1:711-722.
641 Bravo-Cordero, J.J., M. Oser, X. Chen, R. Eddy, L. Hodgson, and J. Condeelis. 2011. A novel
642 spatiotemporal RhoC activation pathway locally regulates cofilin activity at invadopodia. *Curr*
643 *Biol*. 21:635-644.
644 Bu, W., K.B. Lim, Y.H. Yu, A.M. Chou, T. Sudhaharan, and S. Ahmed. 2010. Cdc42 interaction with N-
645 WASP and Toca-1 regulates membrane tubulation, vesicle formation and vesicle motility:
646 implications for endocytosis. *PLoS One*. 5:e12153.
647 Chan Wah Hak, L., S. Khan, I. Di Meglio, A.L. Law, S. Lucken-Ardjomande Hasler, L.M. Quintaneiro, A.P.A.
648 Ferreira, M. Krause, H.T. McMahon, and E. Boucrot. 2018. FBP17 and CIP4 recruit SHIP2 and
649 lamellipodin to prime the plasma membrane for fast endophilin-mediated endocytosis. *Nat Cell*
650 *Biol*. 20:1023-1031.
651 Chander, H., P. Truesdell, J. Meens, and A.W. Craig. 2013. Transducer of Cdc42-dependent actin
652 assembly promotes breast cancer invasion and metastasis. *Oncogene*. 32:3080-3090.
653 Daubon, T., R. Buccione, and E. Génot. 2011. The Aarskog-Scott syndrome protein Fgd1 regulates
654 podosome formation and extracellular matrix remodeling in transforming growth factor β-
655 stimulated aortic endothelial cells. *Mol Cell Biol*. 31:4430-4441.
656 Desmarais, V., H. Yamaguchi, M. Oser, L. Soon, G. Mouneimne, C. Sarmiento, R. Eddy, and J. Condeelis.
657 2009. N-WASP and cortactin are involved in invadopodium-dependent chemotaxis to EGF in
658 breast tumor cells. *Cell Motil Cytoskeleton*. 66:303-316.
659 Di Martino, J., L. Paysan, C. Gest, V. Lagrée, A. Juin, F. Saltel, and V. Moreau. 2014. Cdc42 and Tks5: a
660 minimal and universal molecular signature for functional invadosomes. *Cell Adh Migr*. 8:280-
661 292.
662 Diekmann, R., M. Kahnwald, A. Schoenit, J. Deschamps, U. Matti, and J. Ries. 2020. Optimizing imaging
663 speed and excitation intensity for single-molecule localization microscopy. *Nat Methods*.
664 17:909-912.
665 Diring, J., S. Mouilleron, N.Q. McDonald, and R. Treisman. 2019. RPEL-family rhoGAPs link Rac/Cdc42
666 GTP loading to G-actin availability. *Nat Cell Biol*. 21:845-855.
667 Fay, D.S., and K. Gerow. 2013. A biologist's guide to statistical thinking and analysis. *WormBook*:1-54.
668 García-Mata, R., K. Wennerberg, W.T. Arthur, N.K. Noren, S.M. Ellerbroek, and K. Burridge. 2006.
669 Analysis of activated GAPs and GEFs in cell lysates. *Methods Enzymol*. 406:425-437.
670 Gligorijevic, B., A. Bergman, and J. Condeelis. 2014. Multiparametric classification links tumor
671 microenvironments with tumor cell phenotype. *PLoS Biol*. 12:e1001995.

672 Goicoechea, S.M., B. Bednarski, R. Garcia-Mata, H. Prentice-Dunn, H.J. Kim, and C.A. Otey. 2009. Palladin
673 contributes to invasive motility in human breast cancer cells. *Oncogene*. 28:587-598.
674 Goicoechea, S.M., R. García-Mata, J. Staub, A. Valdivia, L. Sharek, C.G. McCulloch, R.F. Hwang, R. Urrutia,
675 J.J. Yeh, H.J. Kim, and C.A. Otey. 2014. Palladin promotes invasion of pancreatic cancer cells by
676 enhancing invadopodia formation in cancer-associated fibroblasts. *Oncogene*. 33:1265-1273.
677 Goicoechea, S.M., A. Zinn, S.S. Awadia, K. Snyder, and R. Garcia-Mata. 2017. A RhoG-mediated signaling
678 pathway that modulates invadopodia dynamics in breast cancer cells. *J Cell Sci*. 130:1064-1077.
679 Goswami, S., E. Sahai, J.B. Wyckoff, M. Cammer, D. Cox, F.J. Pixley, E.R. Stanley, J.E. Segall, and J.S.
680 Condeelis. 2005. Macrophages promote the invasion of breast carcinoma cells via a colony-
681 stimulating factor-1/epidermal growth factor paracrine loop. *Cancer Res*. 65:5278-5283.
682 Guo, Q., Y. Xiong, Y. Song, K. Hua, and S. Gao. 2019. ARHGAP17 suppresses tumor progression and up-
683 regulates P21 and P27 expression via inhibiting PI3K/AKT signaling pathway in cervical cancer.
684 *Gene*. 692:9-16.
685 Harada, A., B. Furuta, K. Takeuchi, M. Itakura, M. Takahashi, and M. Umeda. 2000. Nadrin, a novel
686 neuron-specific GTPase-activating protein involved in regulated exocytosis. *J Biol Chem*.
687 275:36885-36891.
688 Hartig, S.M., S. Ishikura, R.S. Hicklen, Y. Feng, E.G. Blanchard, K.A. Voelker, C.S. Pichot, R.W. Grange, R.M.
689 Raphael, A. Klip, and S.J. Corey. 2009. The F-BAR protein CIP4 promotes GLUT4 endocytosis
690 through bidirectional interactions with N-WASp and Dynamin-2. *J Cell Sci*. 122:2283-2291.
691 Ho, H.Y., R. Rohatgi, A.M. Lebensohn, M. Le, J. Li, S.P. Gygi, and M.W. Kirschner. 2004. Toca-1 mediates
692 Cdc42-dependent actin nucleation by activating the N-WASP-WIP complex. *Cell*. 118:203-216.
693 Hoshino, D., K.M. Branch, and A.M. Weaver. 2013. Signaling inputs to invadopodia and podosomes. *J*
694 *Cell Sci*. 126:2979-2989.
695 Hoshino, D., J. Jourquin, S.W. Emmons, T. Miller, M. Goldgof, K. Costello, D.R. Tyson, B. Brown, Y. Lu,
696 N.K. Prasad, B. Zhang, G.B. Mills, W.G. Yarbrough, V. Quaranta, M. Seiki, and A.M. Weaver. 2012.
697 Network analysis of the focal adhesion to invadopodia transition identifies a PI3K-PKCα invasive
698 signaling axis. *Sci Signal*. 5:ra66.
699 Hu, J., A. Mukhopadhyay, and A.W. Craig. 2011. Transducer of Cdc42-dependent actin assembly
700 promotes epidermal growth factor-induced cell motility and invasiveness. *J Biol Chem*.
701 286:2261-2272.
702 Juin, A., C. Billottet, V. Moreau, O. Destaing, C. Albiges-Rizo, J. Rosenbaum, E. Genot, and F. Saltel. 2012.
703 Physiological type I collagen organization induces the formation of a novel class of linear
704 invadosomes. *Mol Biol Cell*. 23:297-309.
705 Juin, A., J. Di Martino, B. Leitinger, E. Henriet, A.S. Gary, L. Paysan, J. Bomo, G. Baffet, C. Gauthier-
706 Rouvière, J. Rosenbaum, V. Moreau, and F. Saltel. 2014. Discoidin domain receptor 1 controls
707 linear invadosome formation via a Cdc42-Tuba pathway. *J Cell Biol*. 207:517-533.
708 Kim, S.H., Z. Li, and D.B. Sacks. 2000. E-cadherin-mediated cell-cell attachment activates Cdc42. *J Biol*
709 *Chem*. 275:36999-37005.
710 Kiso, M., S. Tanaka, S. Saji, M. Toi, and F. Sato. 2018. Long isoform of VEGF stimulates cell migration of
711 breast cancer by filopodia formation via NRP1/ARHGAP17/Cdc42 regulatory network. *Int J*
712 *Cancer*.
713 Kreider-Letterman, G., N.M. Carr, and R. Garcia-Mata. 2022a. Fixing the GAP: The role of RhoGAPs in
714 cancer. *Eur J Cell Biol*. 101:151209.
715 Kreider-Letterman, G., M. Cooke, S.M. Goicoechea, M.G. Kazanietz, and R. Garcia-Mata. 2022b.
716 Quantification of ruffle area and dynamics in live or fixed lung adenocarcinoma cells. *STAR*
717 *Protocols*. 3:101437.
718 Lawson, C.D., and A.J. Ridley. 2018. Rho GTPase signaling complexes in cell migration and invasion. *J Cell*
719 *Biol*. 217:447-457.

720 Lorenz, M., H. Yamaguchi, Y. Wang, R.H. Singer, and J. Condeelis. 2004. Imaging sites of N-wasp activity
721 in lamellipodia and invadopodia of carcinoma cells. *Curr Biol*. 14:697-703.
722 Mahlandt, E.K., J.J.G. Arts, W.J. van der Meer, F.H. van der Linden, S. Tol, J.D. van Buul, T.W.J. Gadella,
723 and J. Goedhart. 2021. Visualizing endogenous RhoA activity with an improved localization-
724 based, genetically encoded biosensor. *bioRxiv*:2021.2002.2008.430250.
725 Martin, K.H., K.E. Hayes, E.L. Walk, A.G. Ammer, S.M. Markwell, and S.A. Weed. 2012. Quantitative
726 measurement of invadopodia-mediated extracellular matrix proteolysis in single and
727 multicellular contexts. *J Vis Exp*:e4119.
728 Meirson, T., A. Genna, N. Lukic, T. Makhnii, J. Alter, V.P. Sharma, Y. Wang, A.O. Samson, J.S. Condeelis,
729 and H. Gil-Henn. 2018. Targeting invadopodia-mediated breast cancer metastasis by using ABL
730 kinase inhibitors. *Oncotarget*. 9:22158-22183.
731 Monteiro, P., C. Rossé, A. Castro-Castro, M. Irondelle, E. Lagoutte, P. Paul-Gilloteaux, C. Desnos, E.
732 Formstecher, F. Darchen, D. Perrais, A. Gautreau, M. Hertzog, and P. Chavrier. 2013. Endosomal
733 WASH and exocyst complexes control exocytosis of MT1-MMP at invadopodia. *J Cell Biol*.
734 203:1063-1079.
735 Moreau, V., F. Tatin, C. Varon, and E. Génot. 2003. Actin can reorganize into podosomes in aortic
736 endothelial cells, a process controlled by Cdc42 and RhoA. *Mol Cell Biol*. 23:6809-6822.
737 Moshfegh, Y., J.J. Bravo-Cordero, V. Miskolci, J. Condeelis, and L. Hodgson. 2014. A Trio-Rac1-Pak1
738 signalling axis drives invadopodia disassembly. *Nat Cell Biol*. 16:574-586.
739 Murphy, D.A., and S.A. Courtneidge. 2011. The 'ins' and 'outs' of podosomes and invadopodia:
740 characteristics, formation and function. *Nat Rev Mol Cell Biol*. 12:413-426.
741 Nagy, Z., K. Wynne, A. von Kriegsheim, S. Gambaryan, and A. Smolenski. 2015. Cyclic Nucleotide-
742 dependent Protein Kinases Target ARHGAP17 and ARHGEF6 Complexes in Platelets. *J Biol Chem*.
743 290:29974-29983.
744 Nahidiazar, L., A.V. Agronskaia, J. Broertjes, B. van den Broek, and K. Jalink. 2016. Optimizing Imaging
745 Conditions for Demanding Multi-Color Super Resolution Localization Microscopy. *PLoS One*.
746 11:e0158884.
747 Nakahara, H., S.C. Mueller, M. Nomizu, Y. Yamada, Y. Yeh, and W.T. Chen. 1998. Activation of beta1
748 integrin signaling stimulates tyrosine phosphorylation of p190RhoGAP and membrane-
749 protrusive activities at invadopodia. *J Biol Chem*. 273:9-12.
750 Noll, B., D. Benz, Y. Frey, F. Meyer, M. Lauinger, S.A. Eisler, S. Schmid, P.L. Hordijk, and M.A. Olayioye.
751 2019. DLC3 suppresses MT1-MMP-dependent matrix degradation by controlling RhoB and actin
752 remodeling at endosomal membranes. *J Cell Sci*.
753 Oikawa, T., T. Itoh, and T. Takenawa. 2008. Sequential signals toward podosome formation in NIH-src
754 cells. *J Cell Biol*. 182:157-169.
755 Pan, S., Y. Deng, J. Fu, Y. Zhang, Z. Zhang, X. Ru, and X. Qin. 2018. Tumor Suppressive Role of ARHGAP17
756 in Colon Cancer Through Wnt/beta-Catenin Signaling. *Cell Physiol Biochem*. 46:2138-2148.
757 Pan, S.L., Y.Y. Deng, J. Fu, Y.H. Zhang, Z.J. Zhang, and X.J. Qin. 2022. ARHGAP17 enhances 5-Fluorouracil-
758 induced apoptosis in colon cancer cells by suppressing Rac1. *Neoplasma*.
759 Parrini, M.C., A. Sadou-Dubourgnoux, K. Aoki, K. Kunida, M. Biondini, A. Hatzoglou, P. Poullet, E.
760 Formstecher, C. Yeaman, M. Matsuda, C. Rossé, and J. Camonis. 2011. SH3BP1, an exocyst-
761 associated RhoGAP, inactivates Rac1 at the front to drive cell motility. *Mol Cell*. 42:650-661.
762 Pichot, C.S., C. Arvanitis, S.M. Hartig, S.A. Jensen, J. Bechill, S. Marzouk, J. Yu, J.A. Frost, and S.J. Corey.
763 2010. Cdc42-interacting protein 4 promotes breast cancer cell invasion and formation of
764 invadopodia through activation of N-WASp. *Cancer Res*. 70:8347-8356.
765 Razidlo, G.L., B. Schroeder, J. Chen, D.D. Billadeau, and M.A. McNiven. 2014. Vav1 as a central regulator
766 of invadopodia assembly. *Curr Biol*. 24:86-93.

767 Richnau, N., and P. Aspenstrom. 2001. Rich, a rho GTPase-activating protein domain-containing protein
768 involved in signaling by Cdc42 and Rac1. *J Biol Chem*. 276:35060-35070.
769 Richnau, N., A. Fransson, K. Farsad, and P. Aspenström. 2004. RICH-1 has a BIN/Amphiphysin/Rvsp
770 domain responsible for binding to membrane lipids and tubulation of liposomes. *Biochem*
771 *Biophys Res Commun*. 320:1034-1042.
772 Rossman, K.L., C.J. Der, and J. Sondek. 2005. GEF means go: turning on RHO GTPases with guanine
773 nucleotide-exchange factors. *Nat Rev Mol Cell Biol*. 6:167-180.
774 Sakurai-Yageta, M., C. Recchi, G. Le Dez, J.B. Sibarita, L. Daviet, J. Camonis, C. D'Souza-Schorey, and P.
775 Chavrier. 2008. The interaction of IQGAP1 with the exocyst complex is required for tumor cell
776 invasion downstream of Cdc42 and RhoA. *J Cell Biol*. 181:985-998.
777 Scott, R.W., D. Crighton, and M.F. Olson. 2011. Modeling and imaging 3-dimensional collective cell
778 invasion. *J Vis Exp*.
779 Stoletov, K., and J.D. Lewis. 2015. Invadopodia: a new therapeutic target to block cancer metastasis.
780 *Expert Rev Anticancer Ther*. 15:733-735.
781 Suman, P., S. Mishra, and H. Chander. 2018. High expression of FBP17 in invasive breast cancer cells
782 promotes invadopodia formation. *Med Oncol*. 35:71.
783 Takano, K., K. Toyooka, and S. Suetsugu. 2008. EFC/F-BAR proteins and the N-WASP-WIP complex induce
784 membrane curvature-dependent actin polymerization. *Embo j*. 27:2817-2828.
785 Tian, L., D.L. Nelson, and D.M. Stewart. 2000. Cdc42-interacting protein 4 mediates binding of the
786 Wiskott-Aldrich syndrome protein to microtubules. *J Biol Chem*. 275:7854-7861.
787 Tian, Q., H. Gao, Y. Zhou, L. Zhu, J. Yang, B. Wang, P. Liu, and J. Yang. 2022. RICH1 inhibits breast cancer
788 stem cell traits through activating kinases cascade of Hippo signaling by competing with Merlin
789 for binding to Amot-p80. *Cell Death & Disease*. 13:71.
790 Tonucci, F.M., E. Almada, C. Borini-Etichetti, A. Pariani, F. Hidalgo, M.J. Rico, J. Girardini, C. Favre, J.R.
791 Goldenring, M. Menacho-Marquez, and M.C. Larocca. 2019. Identification of a CIP4 PKA
792 phosphorylation site involved in the regulation of cancer cell invasiveness and metastasis.
793 *Cancer Lett*.
794 Tsujita, K., A. Kondo, S. Kurisu, J. Hasegawa, T. Itoh, and T. Takenawa. 2013. Antagonistic regulation of F-
795 BAR protein assemblies controls actin polymerization during podosome formation. *J Cell Sci*.
796 126:2267-2278.
797 Tsujita, K., S. Suetsugu, N. Sasaki, M. Furutani, T. Oikawa, and T. Takenawa. 2006. Coordination between
798 the actin cytoskeleton and membrane deformation by a novel membrane tubulation domain of
799 PCH proteins is involved in endocytosis. *J Cell Biol*. 172:269-279.
800 Vaughan, E.M., A.L. Miller, H.Y. Yu, and W.M. Bement. 2011. Control of local Rho GTPase crosstalk by
801 Abr. *Curr Biol*. 21:270-277.
802 Vinci, M., C. Box, and S.A. Eccles. 2015. Three-dimensional (3D) tumor spheroid invasion assay. *J Vis*
803 *Exp*:e52686.
804 Wang, J., Y. Feng, X. Chen, Z. Du, S. Jiang, S. Ma, and W. Zou. 2018. SH3BP1-induced Rac-Wave2 pathway
805 activation regulates cervical cancer cell migration, invasion, and chemoresistance to cisplatin. *J*
806 *Cell Biochem*. 119:1733-1745.
807 Wells, C.D., J.P. Fawcett, A. Traweger, Y. Yamanaka, M. Goudreault, K. Elder, S. Kulkarni, G. Gish, C.
808 Virag, C. Lim, K. Colwill, A. Starostine, P. Metalnikov, and T. Pawson. 2006. A Rich1/Amot
809 complex regulates the Cdc42 GTPase and apical-polarity proteins in epithelial cells. *Cell*.
810 125:535-548.
811 Yamaguchi, H. 2012. Pathological roles of invadopodia in cancer invasion and metastasis. *Eur J Cell Biol*.
812 91:902-907.

813 Yamaguchi, H., M. Lorenz, S. Kempiak, C. Sarmiento, S. Coniglio, M. Symons, J. Segall, R. Eddy, H. Miki, T.
814 Takenawa, and J. Condeelis. 2005. Molecular mechanisms of invadopodium formation: the role
815 of the N-WASP-Arp2/3 complex pathway and cofilin. *J Cell Biol*. 168:441-452.
816 Yamamoto, H., M. Sutoh, S. Hatakeyama, Y. Hashimoto, T. Yoneyama, T. Koie, H. Saitoh, K. Yamaya, T.
817 Funyu, T. Nakamura, C. Ohyama, and S. Tsuboi. 2011. Requirement for FBP17 in invadopodia
818 formation by invasive bladder tumor cells. *J Urol*. 185:1930-1938.
819 Yu, X., T. Zech, L. McDonald, E.G. Gonzalez, A. Li, I. Macpherson, J.P. Schwarz, H. Spence, K. Futó, P.
820 Timpson, C. Nixon, Y. Ma, I.M. Anton, B. Visegrády, R.H. Insall, K. Oien, K. Blyth, J.C. Norman, and
821 L.M. Machesky. 2012. N-WASP coordinates the delivery and F-actin-mediated capture of MT1-
822 MMP at invasive pseudopods. *J Cell Biol*. 199:527-544.
823 Zagryazhskaya-Masson, A., P. Monteiro, A.S. Macé, A. Castagnino, R. Ferrari, E. Infante, A. Duperray-
824 Susini, F. Dingli, A. Lanyi, D. Loew, E. Génot, and P. Chavrier. 2020. Intersection of TKS5 and
825 FGD1/CDC42 signaling cascades directs the formation of invadopodia. *J Cell Biol*. 219.
826 Zhang, J., C. Yang, L. Gong, S. Zhu, J. Tian, F. Zhang, Q. Zhu, J. Wang, M. Lan, Y. Li, and W. Zhang. 2019.
827 RICH2, a potential tumor suppressor in hepatocellular carcinoma. *Front Biosci (Landmark Ed)*.
828 24:1363-1376.

829 ## Figure legends

830 **Figure 1. ARHGAP17 negatively regulates invadopodia.**

831 (**A**) Representative micrographs of a SUM159 cell with an invadopodia cluster. Cells were treated with
832 PDBu for 30 minutes and stained for cortactin and F-actin (scale bar for both panels, 5 µm). (**B**) shRNA
833 screen of candidate RhoGAPs in SUM159 cells. Cells stably expressing the indicated shRNAs were
834 treated with PDBu for 30 minutes and stained for cortactin and F-actin as invadopodia markers. Colors
835 represent different RhoGAPs, and individual bars represent unique shRNA targeting sequences. Results
836 are expressed as the percentage of cells with invadopodia from 4 images per condition for a total of
837 7100 cells. (**C**) Western blot of ARHGAP17 expression in SUM159 cells stably expressing non-targeting
838 and ARHGAP17-specific shRNAs. Tubulin was used as a loading control. (**D**) Percentage of cells with
839 invadopodia in CTRL or ARHGAP17 KD SUM159 cells treated with PDBu for 30 minutes. Results are
840 expressed as mean ± S.E.M. of 3 independent experiments in which at least 200 cells per condition per
841 experiment were counted. ***, $p<0.001$. (**E**) Western blot of ARHGAP17 KD and Rescue with shRNA-
842 resistant myc-ARHGAP17 in SUM159 cells. (**F**) Percentage of cells with invadopodia in CTRL, ARHGAP17
843 KD, and Rescue SUM159 cells treated PDBu for 30 minutes. Results are expressed as mean ± S.E.M. of 3
844 independent experiments in which at least 200 cells per condition per experiment were counted. **,
845 $p<0.01$; ns, not significant. (**G**) Representative micrographs of CTRL, ARHGAP17 KD, and Rescue with
846 myc-ARHGAP17 in SUM159 cells. F-actin and cortactin staining were used as markers for invadopodia
847 while myc staining was used to visualize myc-ARHGAP17. Cells were treated with PDBu for 30 minutes
848 before fixation and staining. Arrowheads highlight invadopodia clusters (scale bar, 20 µm).

849 **Figure 2. Loss of ARHGAP17 expression promotes invasion**

850 (**A**) Representative micrographs of a SUM159 cell invadopodia cluster degrading a fluorescent-gelatin
851 and collagen IV substrate. F-actin staining was used as a marker for invadopodia (scale bar for left and
852 right panels, 10 µm). (**B**) Representative micrographs of F-actin-stained SUM159 cells degrading
853 fluorescent-gelatin and collagen IV matrix after 24-hour PDBu treatment (scale bar, 20 µm). (**C**)
854 Quantification of matrix degradation by SUM159 cells. Results are expressed as mean ± S.E.M. of 3

855 independent experiments in which at least 20 random fields-of-view (FOV) per condition per experiment
856 were measured. **, p<0.01; ns, not significant. (**D**) Micrographs of SUM159 spheroids grown with
857 Matrigel to promote invasion and without Matrigel to observe spheroid growth (scale bar, 200 µm). (**E**
858 and **F**) Quantification of spheroid size and quantification of invasion corrected for proliferation. Results
859 are expressed as mean ± S.E.M. of 4 independent experiments in which at least 5 spheroids per
860 condition per experiment were measured. *, p<0.05; ***, p<0.001; ns, not significant. (**G**) Z-view of
861 inverse invasion assay of SUM159 cells expressing Scarlet-CAAX with brightest point projection in the y-
862 axis (scale bar, 20 µm). (**H**) Quantification of area invaded by cells in inverse invasion assay. Invasion was
863 measured at 20 microns above the coverslip. Results are expressed as mean ± S.E.M. of 3 independent
864 experiments in which at least 3 FOV per condition per experiment were measured. *, p<0.05; ***,
865 p<0.001.

866 **Figure 3. ARHGAP17 knockdown increases invadopodia stability and accumulation.**

867 (**A**) Representative micrographs of SUM159 cells stained for F-actin (scale bar, 10 µm) and quantification
868 of percent invadopodia coverage after 30 min PDBu treatment. White dashed lines represent the cell
869 outline and yellow dashed lines represent invadopodia clusters. Results are expressed as mean ± S.E.M.
870 of 3 independent experiments in which at least 30 cells per condition per experiment were counted. *,
871 p<0.05; ns, not significant. (**B**) Time course of percentage of SUM159 cells forming invadopodia after
872 PDBu treatment at different intervals. Results are expressed as mean ± S.E.M. of 3 independent
873 experiments in which at least 200 cells per condition per experiment were counted. (**C**) Example
874 invadopodia dynamics showing assembly, stability, and disassembly phases as indicated by measuring
875 TKS5-mTagBFP2 intensity over time at 30 second intervals after PDBu treatment. Gray line represents a
876 second-order smoothing polynomial. (**D**) Representative micrographs of single invadopodia dynamics of
877 SUM159 cells expressing TKS5-mTagBFP2 as a marker for invadopodia after PDBu treatment (scale bar, 1
878 µm). (**E-H**) Quantification of invadopodia dynamics. Results are expressed as mean ± S.E.M. of 3
879 independent experiments in which at least 12 invadopodia per condition per experiment were
880 measured. Large points represent biological replicates, small points represent technical replicates. *,
881 p<0.05; **, p<0.01; ***, p<0.001; ns, not significant.

882 **Figure 4. ARHGAP17 localizes to invadopodia**

883 (**A**) Representative micrographs of CTRL and ARHGAP17 KO SUM159 cells stained for F-actin and
884 ARHGAP17. Arrowheads highlight invadopodia clusters (scale bar, 10 µm). (**B**) Representative TIRF
885 micrographs of a SUM159 cell expressing TKS5-mTagBFP2 as a marker for invadopodia and ARHGAP17-
886 GFP (expressed in ARHGAP17 KO background) forming an invadopodia cluster after 30 min PDBu
887 treatment (scale bar for both panels, 5 µm). (**C**) STORM reconstructions of SUM159 cells treated with
888 PDBu showing myc-ARHGAP17 (expressed in ARHGAP17 KO background) localization to invadopodia as
889 defined by F-actin staining (scale bar, 1 µm). (**D**) Quantification of STORM reconstructions using the
890 radial intensity analysis of F-actin, myc-ARHGAP17, cortactin, and paxillin in invadopodia. Lines are
891 expressed as mean ± S.E.M. of 3 independent experiments in which at least 20 invadopodia per
892 condition per experiment were measured.

893 **Figure 5. ARHGAP17 targets invadopodia through both the N-BAR and proline-rich domains**

894 (**A**) Domain structure of ARHGAP17 and the ARHGAP17 mutants used in this study. (**B**) Representative
895 TIRF micrographs of individual invadopodia in SUM159 cells expressing ARHGAP17-GFP domain deletion

896 mutants in ARHGAP17 KO cells. Cells were treated with PDBu for 30 min and stained for F-actin as a
897 marker for invadopodia (scale bar, 0.5 µm). (**C**) Radial intensity analysis of F-actin and ARHGAP17-GFP
898 mutants in invadopodia. Lines are expressed as mean ± S.E.M. of 4 independent experiments in which at
899 least 26 invadopodia per condition per experiment were measured. (**D** and **E**) Quantification of
900 ARHGAP17 distance from the center of invadopodia based on peak intensity and quantification of
901 normalized intensity of ARHGAP17 at invadopodia. Results are expressed as mean ± S.E.M. of 4
902 independent experiments in which at least 26 invadopodia per condition per experiment were
903 measured. Large points represent biological replicates, small points represent technical replicates. *,
904 p<0.05; ***, p<0.001. (**F**) Percentage of cells with invadopodia in CTRL, ARHGAP17 KO, and Rescue with
905 ARHGAP17 domain deletion mutants after 30 minutes PDBu treatment. Results are expressed as mean ±
906 S.E.M. of 3 independent experiments in which at least 200 cells per condition per experiment were
907 counted. Statistical analysis is a 1-way ANOVA with a Tukey's post hoc test. Different letters indicate
908 significant differences between conditions as defined by p<0.05.

909 **Figure 6. ARHGAP17 Cdc42-specific catalytic activity is required for its function at invadopodia**

910 (**A**) Pulldown of endogenous ARHGAP17 in SUM159 cells using constitutively active RhoA (Q63L), Rac1
911 (Q61L), and Cdc42 (Q61L) tagged with Glutathione S-transferase (GST) or with GST alone. (**B**) Pulldown
912 of active Cdc42 using the p21 binding domain (PBD) of p21 activated kinase 1 protein (PAK). Results are
913 expressed as mean ± S.E.M. of 4 independent experiments. ***, p<0.001; ns, not significant. (**C**) PBD
914 pulldown of active Cdc42 in SUM159 cells after treatment with PDBu at the indicated time points. Left
915 panel shows a representative WB; right panel shows the quantification of 3 independent experiments.
916 Results are expressed as mean ± S.E.M. *, p<0.05; ns, not significant. (**D**) Representative TIRF
917 micrographs of ARHGAP17 KO SUM159 cells forming single invadopodia after PDBu treatment stained
918 for F-actin as a marker for invadopodia and expressing either WT or catalytic dead (CD) ARHGAP17-GFP
919 (expressed in ARHGAP17 KO background) (scale bar, 0.5 µm). (**E**) Radial intensity analysis of F-actin, WT
920 ARHGAP17-GFP, and CD ARHGAP17-GFP in invadopodia. Lines are expressed as mean ± S.E.M. of 3
921 independent experiments in which at least 40 invadopodia per condition per experiment were
922 measured. (**F** and **G**) Quantification of ARHGAP17-GFP distance from the center of invadopodia based on
923 peak intensity and normalized intensity of ARHGAP17 at invadopodia. Results are expressed as mean ±
924 S.E.M. of 3 independent experiments in which at least 40 invadopodia per condition per experiment
925 were measured. Large points represent biological replicates, small points represent technical replicates.
926 ns, not significant. (**H**) Percentage of cells with invadopodia in CTRL, ARHGAP17 KO, and Rescue with
927 either WT or CD ARHGAP17-GFP after 30 minutes PDBu treatment. Results are expressed as mean ±
928 S.E.M. of 3 independent experiments in which at least 200 cells per condition per experiment were
929 counted. **, p<0.01; ns, not significant.

930 **Figure 7. ARHGAP17regulates the spatiotemporal dynamics of Cdc42 activity during invadopodia**
931 **turnover**

932 (**A**) Design of the Cdc42 activity biosensor used in this study, composed of the GTPase-binding domain of
933 WASP (wGBD) tagged with dTomato. (**B**) Representative TIRF micrographs of a SUM159 cell expressing
934 TKS5-mTagBFP2 as a marker for invadopodia and dTomato-wGBD as a marker for Cdc42 activity and
935 forming an invadopodia cluster after PDBu treatment (scale bar for both panels, 5 µm). (**C**)
936 Representative TIRF micrographs of a SUM159 cell forming an individual invadopodia after PDBu
937 treatment. Cells were expressing TKS5-mTagBFP2 as a marker for invadopodia, ARHGAP17-GFP

938 (expressed in ARHGAP17 KO background), and dTomato-wGBD as a marker for Cdc42 activity (scale bar,
939 1 µm). (**D**) Quantification of TKS5-mTagBFP2, ARHGAP17-GFP (expressed in ARHGAP17 KO background),
940 and dTomato-wGBD intensity at individual invadopodia. Intensity and time have been rescaled between
941 values of 0 and 1 for each invadopodia to allow for comparison. Lines are loess smoothing and 95%
942 confidence from 3 independent experiments in which at least 10 invadopodia per condition per
943 experiment were measured. (**E**) Cross-correlation analysis of TKS5-mTagBFP2, ARHGAP17-GFP
944 (expressed in ARHGAP17 KO background), and dTomato-wGBD intensity. Higher values denote positive
945 correlation and lag denotes the time shift effect on correlation between signals. Lines are loess
946 smoothing and 95% confidence from 3 independent experiments in which at least 10 invadopodia per
947 condition per experiment were measured. (**F**) Quantification of the peak dTomato-wGBD intensity at
948 individual invadopodia after PDBu treatment, normalized to the average whole-cell intensity before
949 treatment. Results are expressed as mean ± S.E.M. of 3 independent experiments. Large points
950 represent biological replicates, small points represent technical replicates. *, $p<0.05$; ns, not significant.
951 (**G**) Radial intensity profiles of individual invadopodia from live cells expressing TKS5-mTagBFP2,
952 ARHGAP17-GFP (expressed in ARHGAP17 KO background), and dTomato-wGBD plotted over time. Time
953 scales between invadopodia are rescaled between 0 and 1 to allow for alignment of intensity values.
954 Results are expressed as the mean of 8 representative invadopodia from 4 independent experiments. (**H**
955 and **I**) Radial profile plots taken from time 0.25 and 0.75 of panel (**G**) showing relative intensity and
956 localization of the invadopodia markers while the invadopodia are assembling and disassembling,
957 respectively. Results are expressed as mean ± S.E.M. of 8 invadopodia from 4 independent experiments.

958 **Figure 8. ARHGAP17 interacts with CIP4 to regulate invadopodia**

959 (**A**) Representative western blot of CIP4 expression in SUM159 cells expressing non-targeting (CTRL) or
960 CIP4-specific shRNAs. (**B**) Representative micrographs of CTRL and CIP4 KD (shRNA #4) SUM159 cells. F-
961 actin and cortactin staining were used as markers for invadopodia. Cells were treated with PDBu for 30
962 minutes before fixation and staining. Arrowheads highlight invadopodia clusters (scale bar, 20 µm). (**C**)
963 Percentage of cells with invadopodia in CTRL and CIP4 KD SUM159 cells treated PDBu for 30 minutes.
964 Results are expressed as mean ± S.E.M. of 3 independent experiments in which at least 200 cells per
965 condition per experiment were counted. *, $p<0.05$; **, $p<0.01$. (**D**) Representative micrographs of
966 SUM159 cells treated with PDBu for 30 min and stained for F-actin and endogenous CIP4 (scale bar, 10
967 µm). (**E**) Radial intensity analysis of F-actin and CIP4 in invadopodia. Lines are expressed as mean ±
968 S.E.M. of 3 independent experiments in which at least 10 invadopodia per condition per experiment
969 were measured. (**F**) Western blot of co-immunoprecipitation of endogenous ARHGAP17 and CIP4 in
970 SUM159 cells. (**G**) Western blot of co-immunoprecipitation of myc-CIP4 with GFP, ΔC ARHGAP17-GFP, or
971 WT ARHGAP17-GFP. (**H**) Western blot of affinity precipitation of myc-CIP4 and CD ARHGAP17-GFP using
972 GST-Cdc42-Q61L bound to Glutathione Sepharose 4B.

973 **Figure 9. Spatiotemporal dynamics of CIP4 and ARHGAP17**

974 (**A**) Representative TIRF micrographs of a SUM159 cell forming a single invadopodia after PDBu
975 treatment expressing TKS5-mTagBFP2 as a marker for invadopodia, CIP4-GFP (expressed in CIP4 KD
976 background), and dTomato-wGBD as a marker for Cdc42 activity (scale bar, 0.5 µm). (**B**) Quantification
977 of TKS5-mTagBFP2, CIP4-GFP (expressed in CIP4 KD background), and dTomato-wGBD intensity at
978 individual invadopodia. Intensity and time were rescaled between values of 0 and 1 for each
979 invadopodia to allow for comparison. Lines are loess smoothing and 95% confidence from 3

980 independent experiments in which at least 10 invadopodia per condition per experiment were
981 measured. (**C**) Cross-correlation analysis of TKS5-mTagBFP2, CIP4-GFP (expressed in CIP4 KD
982 background), and dTomato-wGBD intensity. Higher values denote positive correlation and lag denotes
983 the time shift effect on correlation between signals. Lines are loess smoothing and 95% confidence from
984 3 independent experiments in which at least 10 invadopodia per condition per experiment were
985 measured. (**D**) Representative TIRF micrographs of ARHGAP17 KO SUM159 cells transfected with the
986 indicated constructs and treated with PDBu for 30 min. Cells were fixed and stained for F-actin and myc
987 to detect myc-CIP4 (scale bar, 10 µm). (**E**) Radial intensity analysis of F-actin, ARHGAP17-GFP, and myc-
988 CIP4 in invadopodia. Lines are expressed as mean ± S.E.M. of 3 independent experiments in which at
989 least 10 invadopodia per condition per experiment were measured. (**F**) Van Steensil's cross-correlation
990 function of ARHGAP17-GFP colocalization with myc-CIP4 or the background signal of the anti-myc
991 antibody at invadopodia clusters in SUM159 cells treated with PDBu for 30 min. Shift denotes the x-
992 dimension movement of one channel in relation to the other. Lines are loess smoothing and 95%
993 confidence from 3 independent experiments in which at least 10 invadopodia clusters per condition per
994 experiment were measured. (**G**) Invadopodia assay of SUM159 cells after 30 minutes PDBu treatment in
995 which CIP4 and ARHGAP17 were either silenced and/or overexpressed in all possible combinations as
996 indicated in the graph. Results are expressed as mean ± S.E.M. of 3 independent experiments in which at
997 least 200 cells per condition per experiment were counted. Statistical analysis is a 1-way ANOVA with a
998 Tukey's post hoc test. Different letters indicate significant differences between conditions as defined by
999 $p<0.05$.

1000 **Figure 10. Model of ARHGAP17 function in invadopodia**

1001 During invadopodia assembly/maturation, ARHGAP17 is present at the invadopodia ring, which helps to
1002 restrict Cdc42 activity to the invadopodia core. Cdc42 is activated by a specific GEF at the invadopodia
1003 core, most likely FGD1, where it promotes actin nucleation through binding to N-WASP and CIP4 and
1004 stimulates degradation through its interaction with IQGAP. During disassembly, ARHGAP17 moves to the
1005 invadopodia core by binding to CIP4 where it inactivates Cdc42.

1006 Video figure legends

1007 **Figure 1–video 1. SUM159 cell forming invadopodia after PDBu treatment**

1008 Live TIRF imaging of a SUM159 cell expressing TKS5-mTagBFP2 and treated with PDBu (scale bar, 10
1009 µm).

1010 **Figure 4–video 1. ARHGAP17 localizes to invadopodia**

1011 Live TIRF imaging of a SUM159 cell expressing TKS5-mTagBFP2 and ARHGAP17-GFP (expressed in
1012 ARHGAP17 KO background), treated with PDBu (scale bar, 10 µm).

1013 **Figure 7–video 1. Cdc42 activity at invadopodia.**

1014 Live TIRF of a SUM159 cell expressing TKS5-mTagBFP2 and dTomato-wGBD, treated with PDBu (scale
1015 bar, 10 µm).

1016 **Figure 7–video 2. Localization of ARHGAP17 and Cdc42 activity at an individual invadopodia.**

1017 Live TIRF of an individual invadopodia from a SUM159 cells expressing TKS5-mTagBFP2, ARHGAP17-GFP
1018 (expressed in ARHGAP17 KO background), and dTomato-wGBD, treated with PDBu (scale bar, 1 µm).

1019 **Figure 9–video 1. Localization of CIP4 and Cdc42 activity at an individual invadopodia.**

1020 Live TIRF of an individual invadopodia from a SUM159 cells expressing TKS5-mTagBFP2, GFP-CIP4, and
1021 dTomato-wGBD, treated with PDBu (scale bar, 1 µm).

1022 Supplementary figure legends

1023 **Figure 1-figure supplement 1. ARHGAP17 KO validation**

1024 (**A**) Representative western blot showing loss of ARHGAP17 protein in SUM159 cells using two different
1025 gRNA targets. (**B**) Percentage of cells with invadopodia after treatment with PDBu for 30 minutes.
1026 Results are expressed as mean ± S.E.M. of 3 independent experiments in which at least 200 cells per
1027 condition per experiment were counted. **, p<0.01.

1028 **Figure 1-figure supplement 2. ARHGAP17 KD increases the formation of spontaneous invadopodia**

1029 (**A**) Representative micrographs of ARHGAP17 knockdown and Rescue with shRNA resistant myc-
1030 ARHGAP17 in SUM159 cells. F-actin and cortactin staining were used as markers for invadopodia while
1031 myc staining was used to visualize myc-ARHGAP17. Arrowheads highlight invadopodia clusters (scale
1032 bar, 20 µm). (**B**) Percentage of cells with invadopodia after treatment with PDBu for 30 minutes. Results
1033 are expressed as mean ± S.E.M. of 3 independent experiments in which at least 200 cells per condition
1034 per experiment were counted. **, p<0.01; ns, not significant.

1035 **Figure 3-figure supplement 1. ARHGAP17 KD reduces invadopodia turnover**

1036 (**A**) Quantification of change in percentage of cells forming invadopodia between peak invadopodia
1037 formation 10 minutes after PDBu treatment and equilibrium at 30 minutes after PDBu treatment.
1038 Results are expressed as mean ± S.E.M. of 3 independent experiments in which at least 200 cells per
1039 condition per experiment were counted. *, p<0.05; **, p<0.01; ns, not significant.

1040 **Figure 3-figure supplement 2. ARHGAP17 regulates invadopodia lifetime and stability**

1041 (**A** and **B**) Quantification of invadopodia dynamics. Results are expressed as mean ± S.E.M. of 3
1042 independent experiments. Large points represent biological replicates, small points represent technical
1043 replicates. ns, not significant. (**C**) Principal component analysis of invadopodia dynamics. Circles
1044 represent 95% confidence.

1045 **Figure 4-figure supplement 1. Paxillin and cortactin localization to invadopodia**

1046 (**A** and **B**) STORM reconstructions of SUM159 cells treated with PDBu showing cortactin and paxillin
1047 localization to invadopodia as defined by F-actin staining (scale bar, 1 µm).

1048 **Figure 6-figure supplement 1. Cdc42 activity in ARHGAP17 KD cells**

1049 (**A**) PBD pulldown of active Cdc42 in ARHGAP17 KD SUM159 cells after treatment with PDBu at the
1050 indicated time points. Results are expressed as mean ± S.E.M. of 3 independent experiments. *, p<0.05;
1051 ns, not significant.

1052 **Figure 7-figure supplement 1. Validation of the Cdc42 biosensor specificity**

1053 (**A**) Representative micrographs of SUM159 showing colocalization of the dTomato-wGBD sensor with
1054 different mTurquoise2-H2A-RhoGTPase-ΔCAAX constructs (RhoA-G14V, Rac1-G12V, or Cdc42-G12V)
1055 (scale bar, 10 µm). (**B**) Quantification of the average intensity of dTomato-wGBD signal within the
1056 nucleus ratioed to the average intensity in the cytosol. Results are mean ± S.D. of at least 14 cells per
1057 condition from 3 independent experiments.

Fig. 1

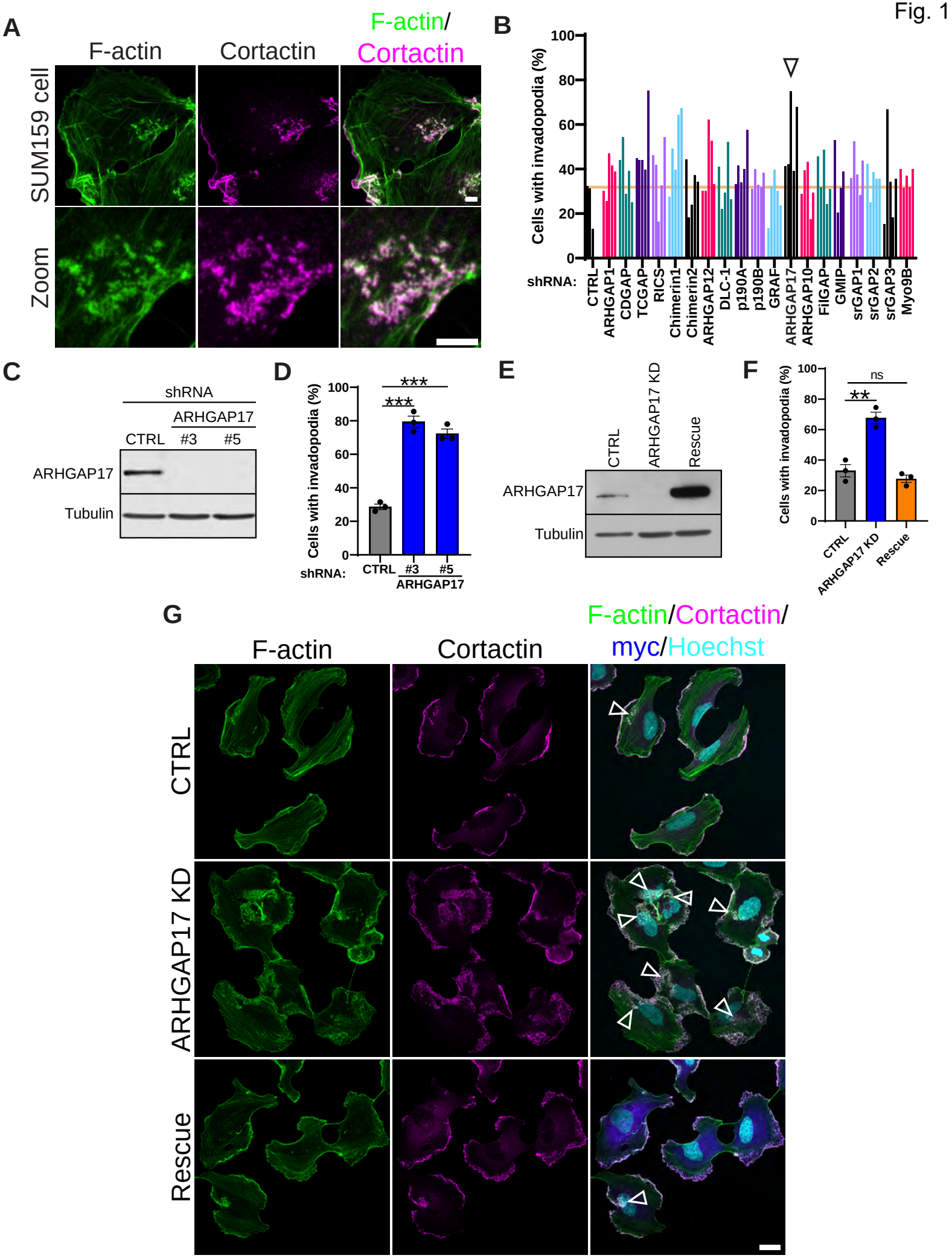
A
F-actin
Cortactin
F-actin/
Cortactin
SUM159 cell
Zoom
B
Cells with invadopodia (%)
shRNA:
CTRL
ARHGAP1
CDGAP
TCGAP
RICS
Chimerin1
Chimerin2
ARHGAP12
DLC-1
p190A
p190B
GRAF
ARHGAP17
ARHGAP10
FilGAP
GMIP
srGAP1
srGAP2
srGAP3
Myo9B
C
shRNA
ARHGAP17
CTRL
#3
#5
ARHGAP17
Tubulin
D
Cells with invadopodia (%)
***
***
shRNA:
CTRL
#3
#5
ARHGAP17
E
CTRL
ARHGAP17 KD
Rescue
ARHGAP17
Tubulin
F
Cells with invadopodia (%)
ns
**
CTRL
ARHGAP17 KD
Rescue
G
F-actin
Cortactin
F-actin/Cortactin/
myc/Hoechst
CTRL
ARHGAP17 KD
Rescue

Figure 1 - figure supplement 1

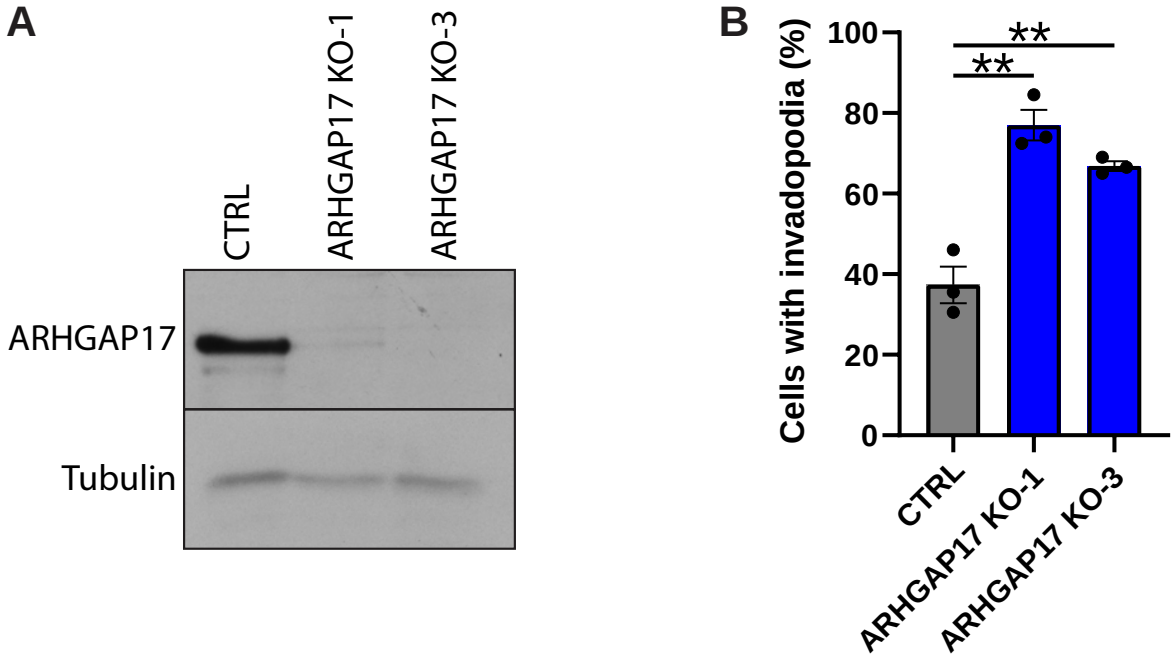

Figure 1 - figure supplement 2

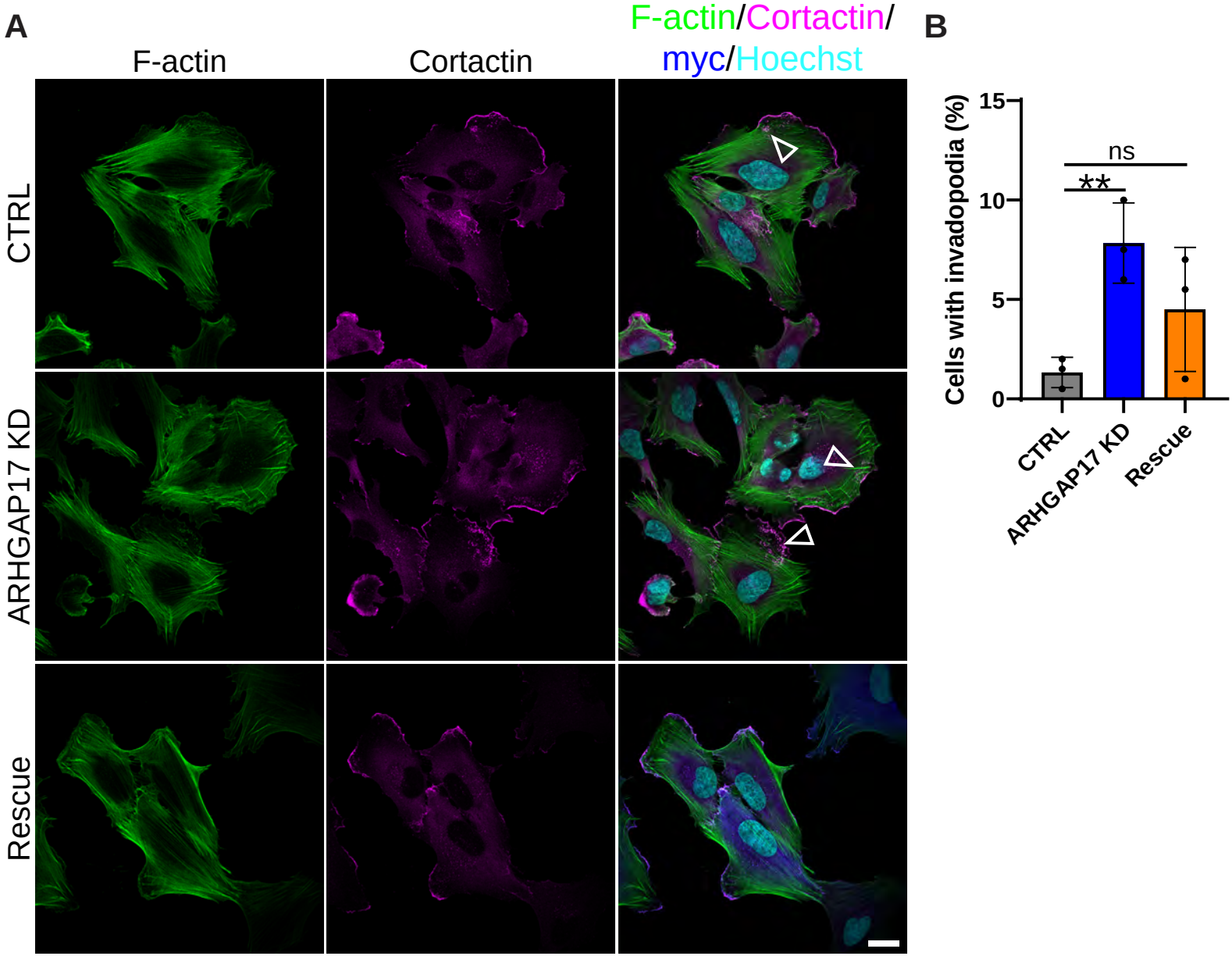

Fig. 2

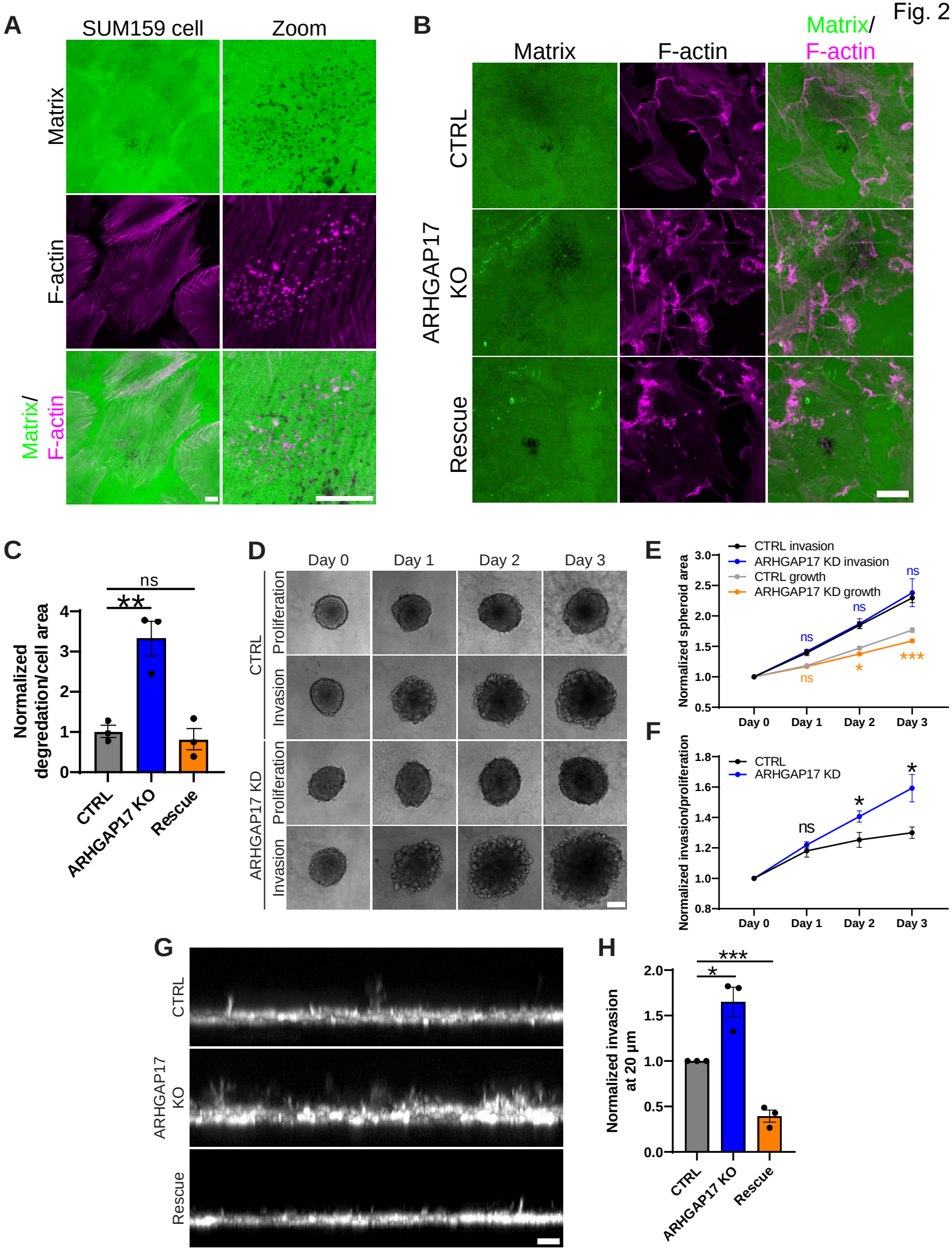
A
SUM159 cell
Zoom
Matrix
F-actin
Matrix/
F-actin
B
Matrix
F-actin
Matrix/
F-actin
CTRL
ARHGAP17
KO
Rescue
C
ns
**
Normalized
degredation/cell area
CTRL
ARHGAP17 KO
Rescue
D
Day 0
Day 1
Day 2
Day 3
CTRL
Proliferation
Invasion
ARHGAP17 KD
Proliferation
Invasion
E
CTRL invasion
ARHGAP17 KD invasion
CTRL growth
ARHGAP17 KD growth
Normalized spheroid area
ns
ns
ns
ns
*
***
Day 0
Day 1
Day 2
Day 3
F
CTRL
ARHGAP17 KD
Normalized invasion/proliferation
ns
*
*
Day 0
Day 1
Day 2
Day 3
G
CTRL
ARHGAP17
KO
Rescue
H
***
*
Normalized invasion
at 20 µm
CTRL
ARHGAP17 KO
Rescue

Fig. 3

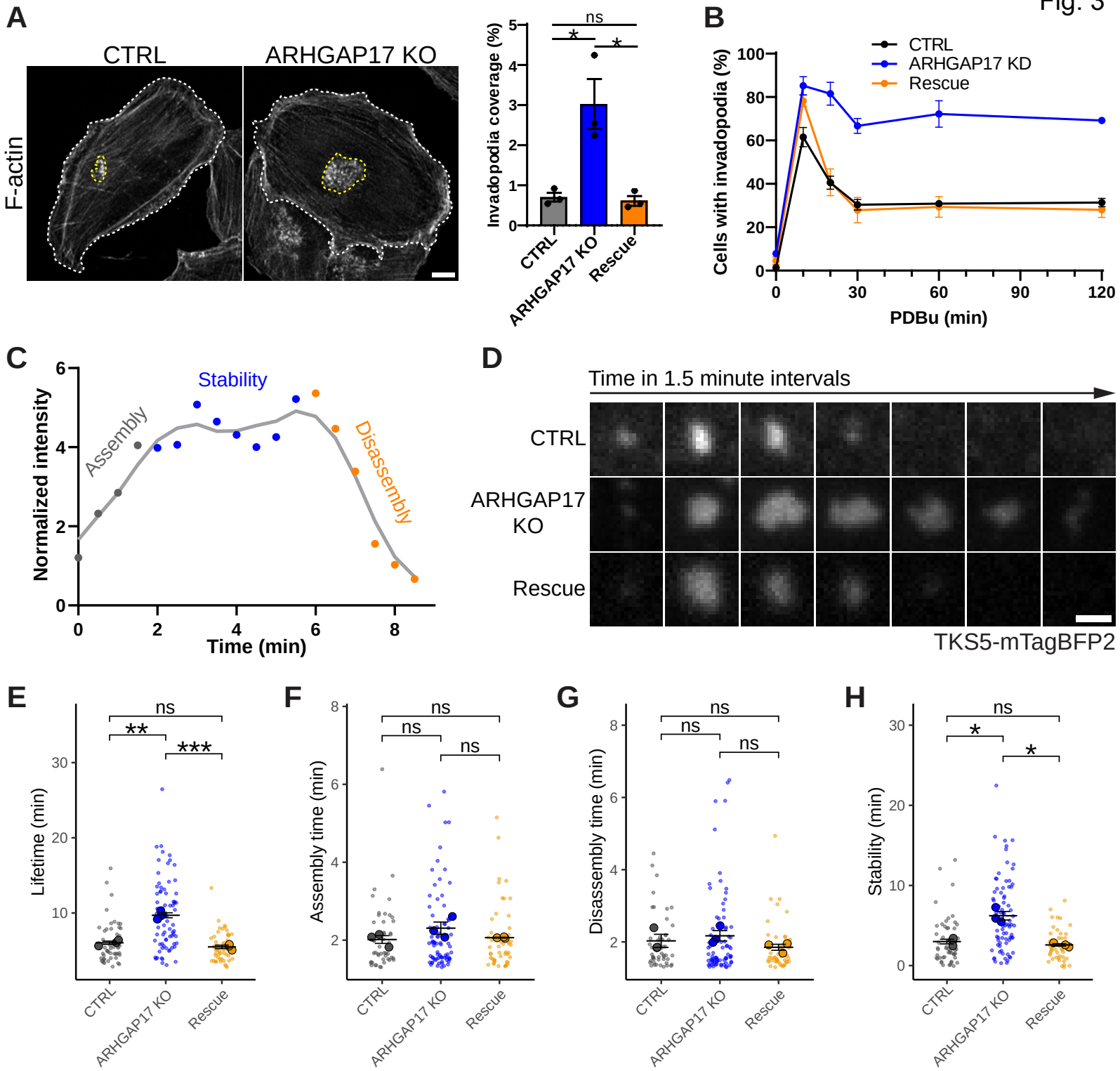
A
CTRL
ARHGAP17 KO
F-actin
Invadopodia coverage (%)
ns
*
*
CTRL
ARHGAP17 KO
Rescue
B
CTRL
ARHGAP17 KD
Rescue
Cells with invadopodia (%)
PDBu (min)
C
Stability
Assembly
Disassembly
Normalized intensity
Time (min)
D
Time in 1.5 minute intervals
CTRL
ARHGAP17 KO
Rescue
TKS5-mTagBFP2
E
Lifetime (min)
ns
**
***
F
Assembly time (min)
ns
ns
ns
G
Disassembly time (min)
ns
ns
ns
H
Stability (min)
ns
*
*
CTRL
ARHGAP17 KO
Rescue

Figure 3 - figure supplement 1

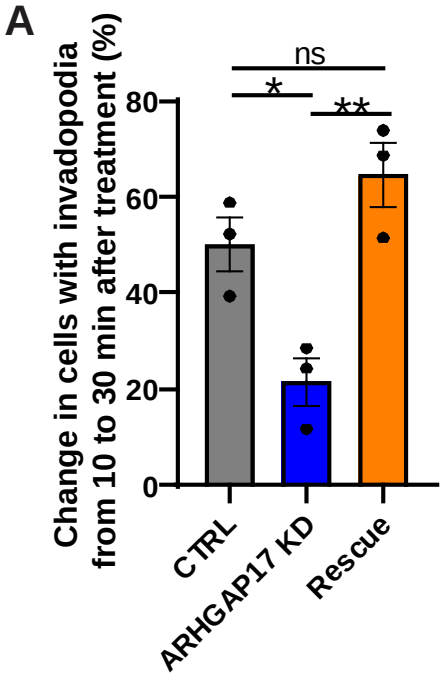

Figure 3 - figure supplement 2

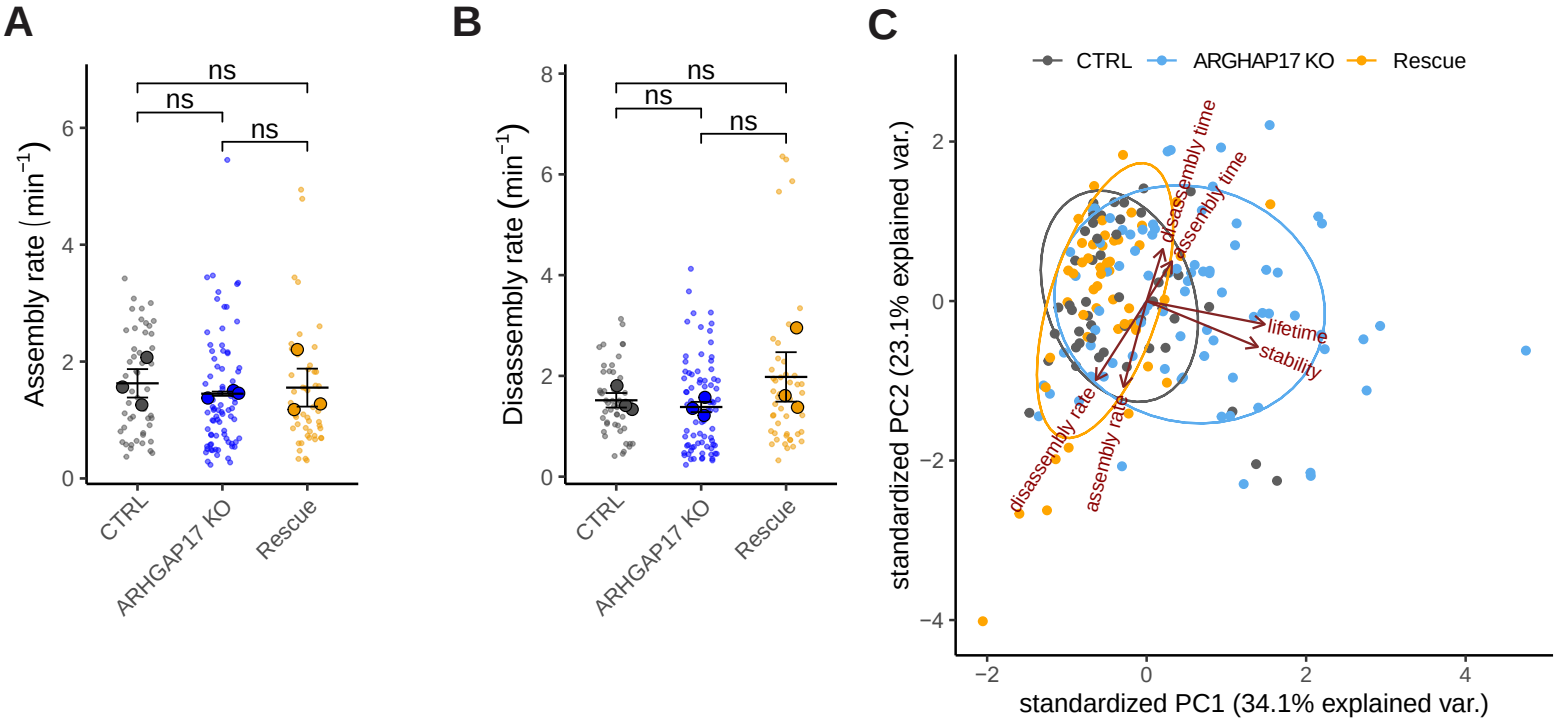

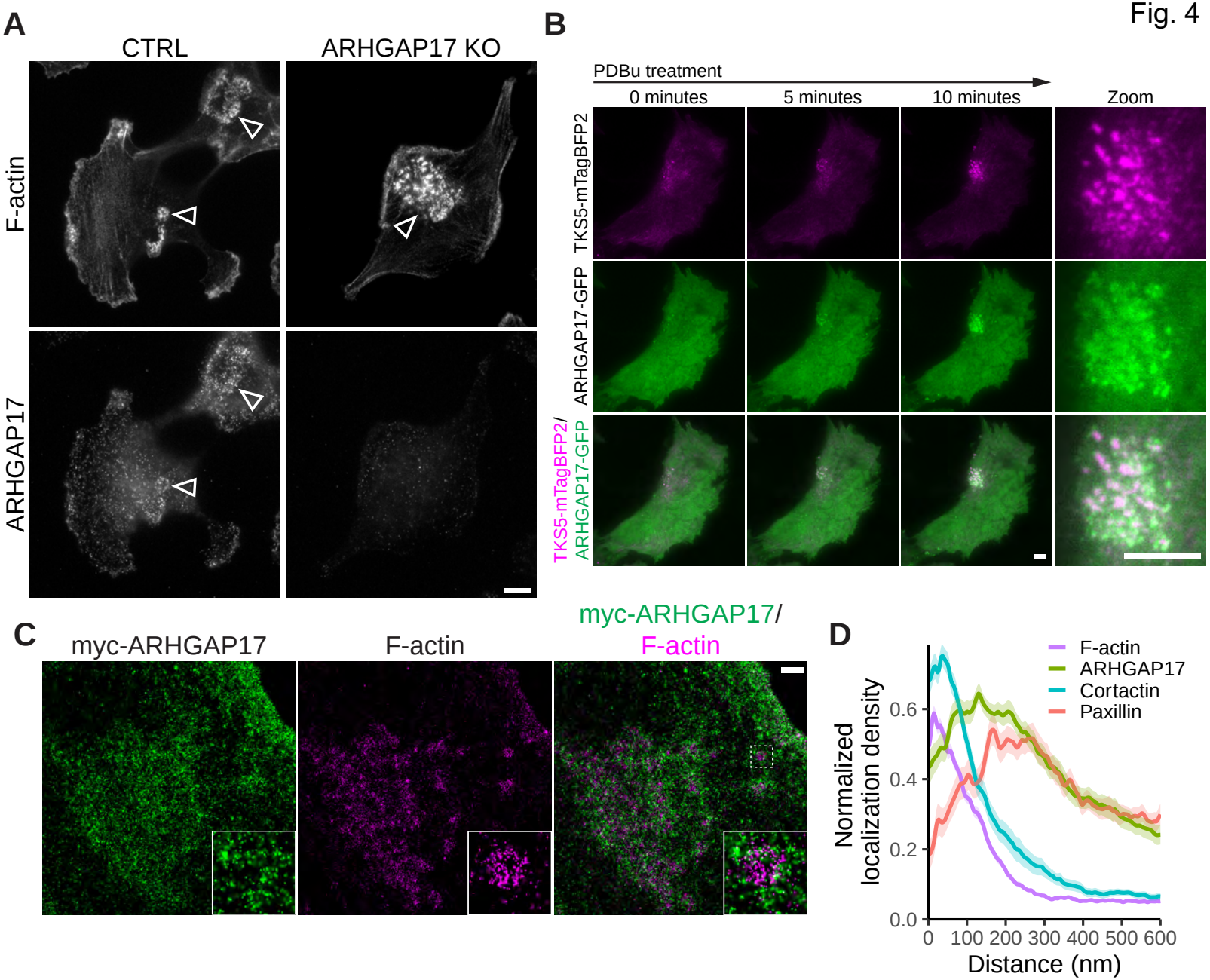
A
CTRL
ARHGAP17 KO
F-actin
ARHGAP17
B
PDBu treatment
0 minutes
5 minutes
10 minutes
Zoom
TKS5-mTagBFP2
ARHGAP17-GFP
TKS5-mTagBFP2/
ARHGAP17-GFP
C
myc-ARHGAP17
F-actin
myc-ARHGAP17/
F-actin
D
F-actin
ARHGAP17
Cortactin
Paxillin
Normalized
localization density
0.0
0.2
0.4
0.6
0
100
200
300
400
500
600
Distance (nm)

Figure 4 - figure supplement 1

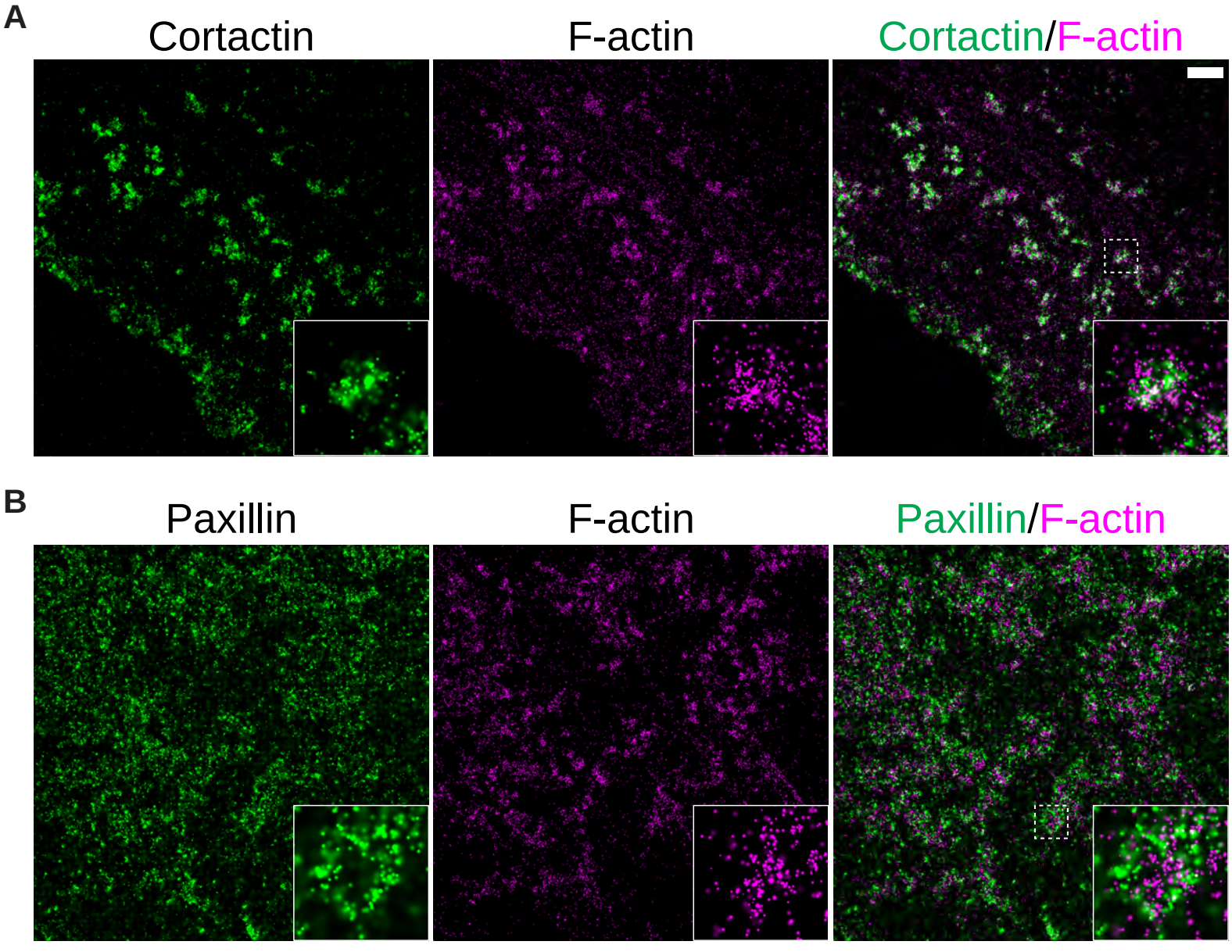

Fig. 5

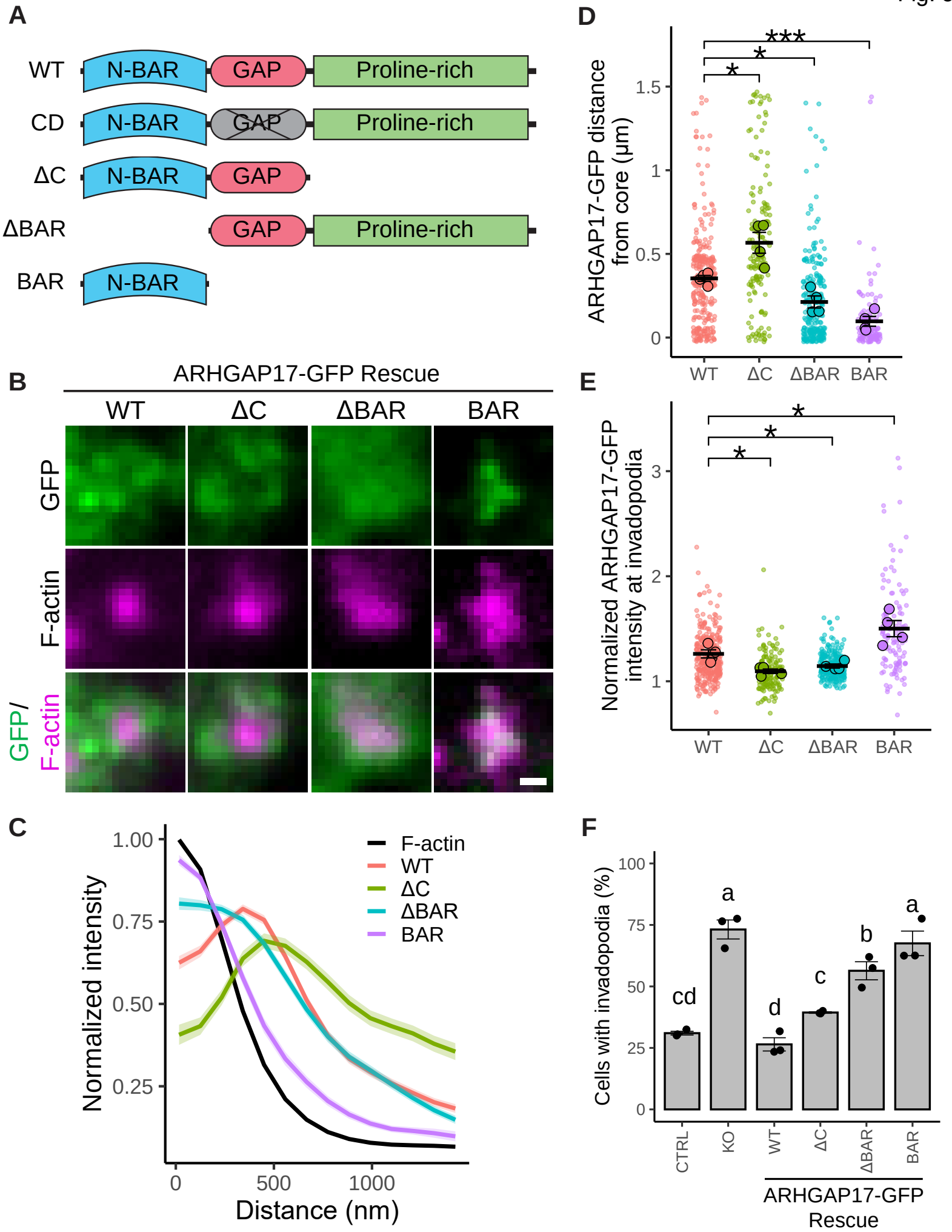
A
WT
N-BAR
GAP
Proline-rich
CD
N-BAR
GAP
Proline-rich
ΔC
N-BAR
GAP
ΔBAR
GAP
Proline-rich
BAR
N-BAR
B
ARHGAP17-GFP Rescue
WT
ΔC
ΔBAR
BAR
GFP
F-actin
GFP/
F-actin
C
Normalized intensity
1.00
0.75
0.50
0.25
0
500
1000
Distance (nm)
F-actin
WT
ΔC
ΔBAR
BAR
D
ARHGAP17-GFP distance from core (µm)
1.5
1
0.5
0
***
*
*
WT
ΔC
ΔBAR
BAR
E
Normalized ARHGAP17-GFP intensity at invadopodia
3
2
1
*
*
*
WT
ΔC
ΔBAR
BAR
F
Cells with invadopodia (%)
100
75
50
25
0
cd
a
d
c
b
a
CTRL
KO
WT
ΔC
ΔBAR
BAR
ARHGAP17-GFP Rescue

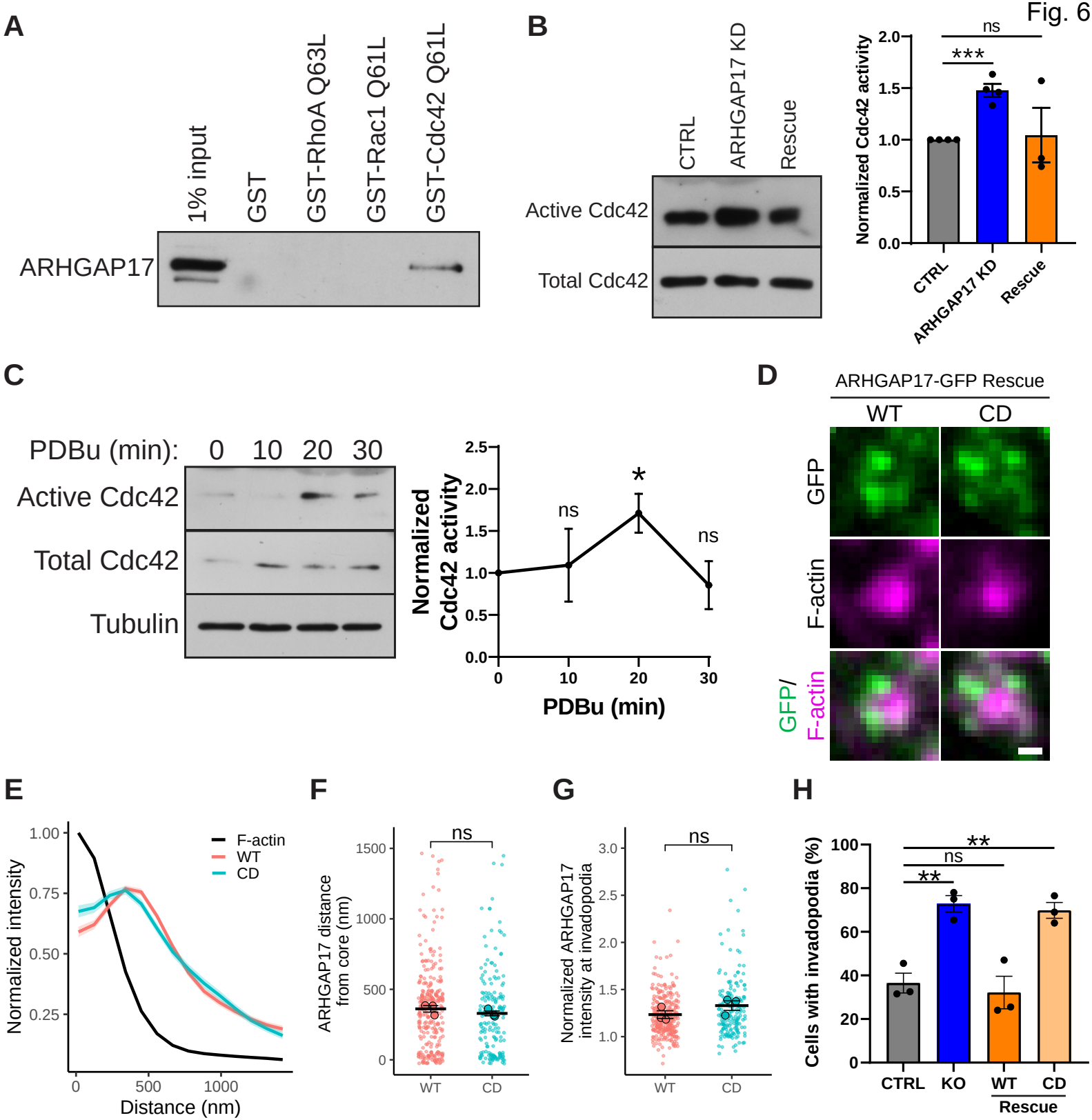
A
1% input
GST
GST-RhoA Q63L
GST-Rac1 Q61L
GST-Cdc42 Q61L
ARHGAP17
B
CTRL
ARHGAP17 KD
Rescue
Active Cdc42
Total Cdc42
Normalized Cdc42 activity
ns
***
CTRL
ARHGAP17 KD
Rescue
C
PDBu (min): 0 10 20 30
Active Cdc42
Total Cdc42
Tubulin
Normalized Cdc42 activity
ns
*
ns
PDBu (min)
D
ARHGAP17-GFP Rescue
WT
CD
GFP
F-actin
GFP/ F-actin
E
F-actin
WT
CD
Normalized intensity
Distance (nm)
F
ARHGAP17 distance from core (nm)
ns
WT
CD
G
Normalized ARHGAP17 intensity at invadopodia
ns
WT
CD
H
Cells with invadopodia (%)
**
ns
**
CTRL
KO
WT
CD
Rescue

Figure 6 - figure supplement 1

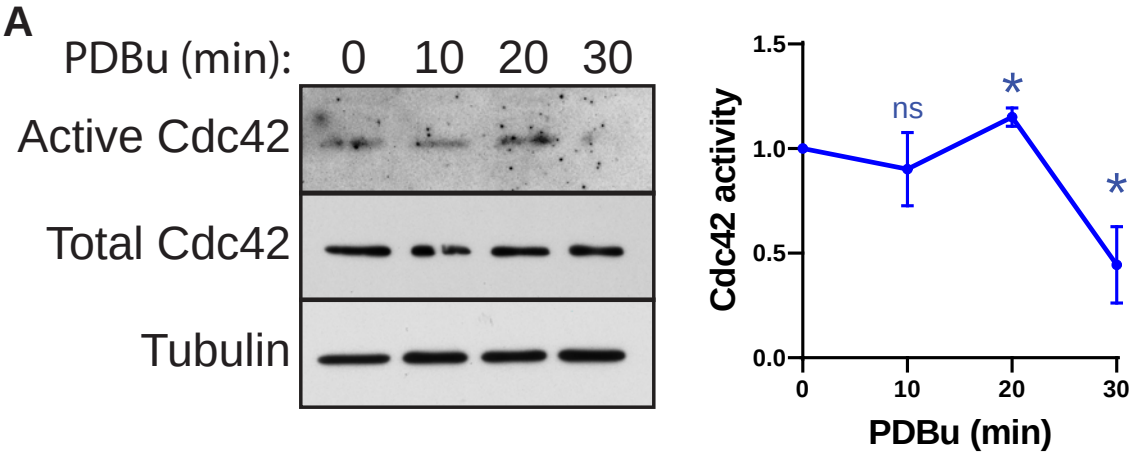

Fig. 7

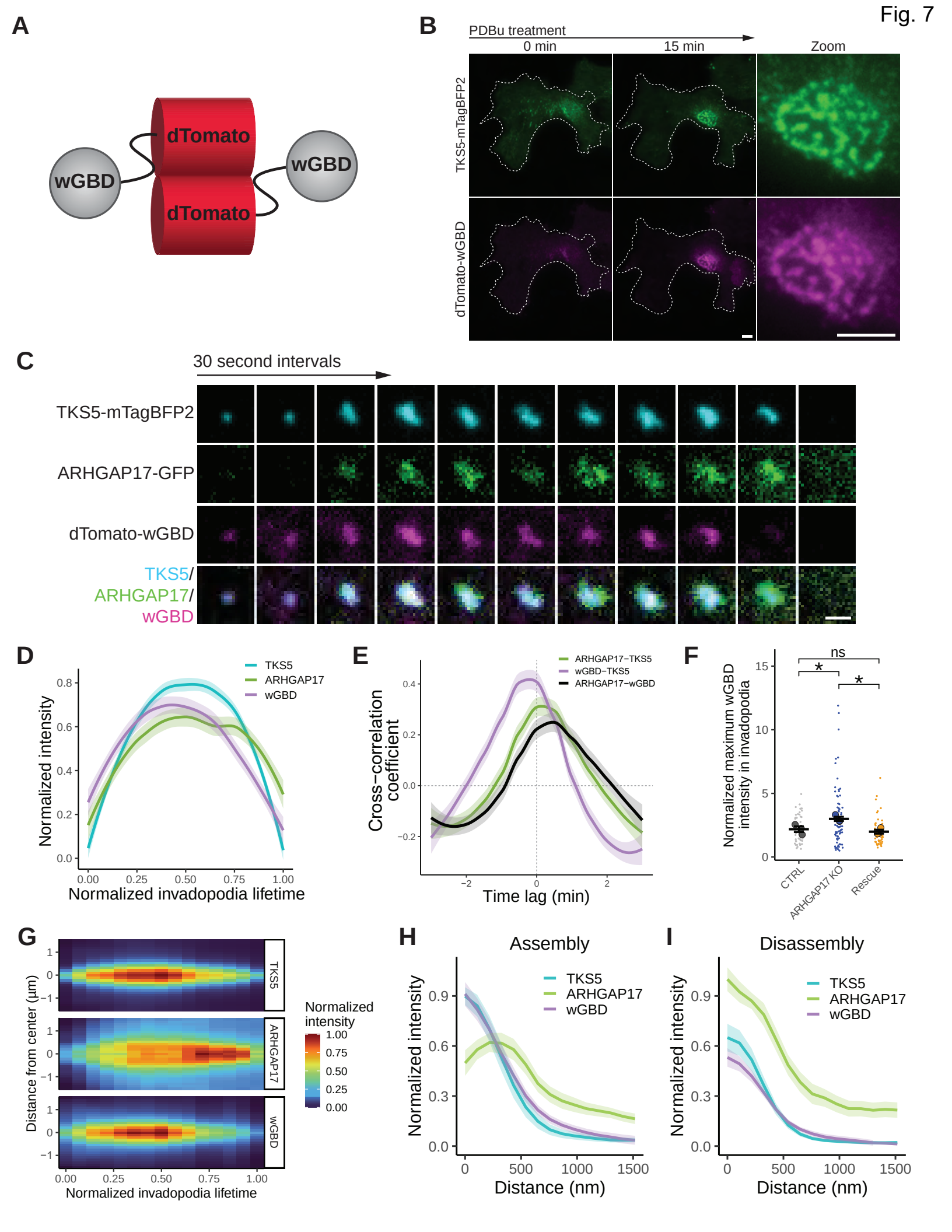
A
dTomato
dTomato
wGBD
wGBD
B
PDBu treatment
0 min
15 min
Zoom
TKS5-mTagBFP2
dTomato-wGBD
C
30 second intervals
TKS5-mTagBFP2
ARHGAP17-GFP
dTomato-wGBD
TKS5/
ARHGAP17/
wGBD
D
TKS5
ARHGAP17
wGBD
Normalized intensity
Normalized invadopodia lifetime
E
ARHGAP17−TKS5
wGBD−TKS5
ARHGAP17−wGBD
Cross−correlation coefficient
Time lag (min)
F
ns
*
*
Normalized maximum wGBD intensity in invadopodia
CTRL
ARHGAP17 KO
Rescue
G
Distance from center (µm)
TKS5
ARHGAP17
wGBD
Normalized intensity
Normalized invadopodia lifetime
H
Assembly
TKS5
ARHGAP17
wGBD
Normalized intensity
Distance (nm)
I
Disassembly
TKS5
ARHGAP17
wGBD
Normalized intensity
Distance (nm)

Figure 7 - figure supplement 1

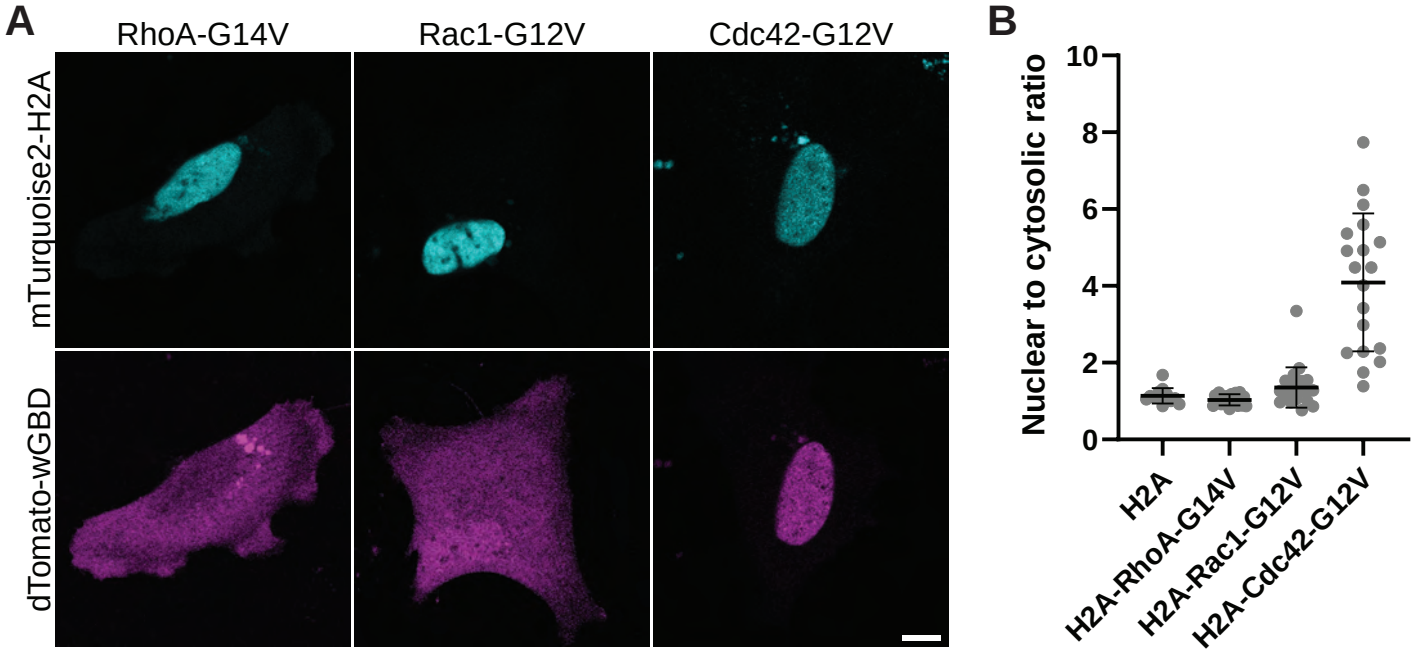

Fig. 8

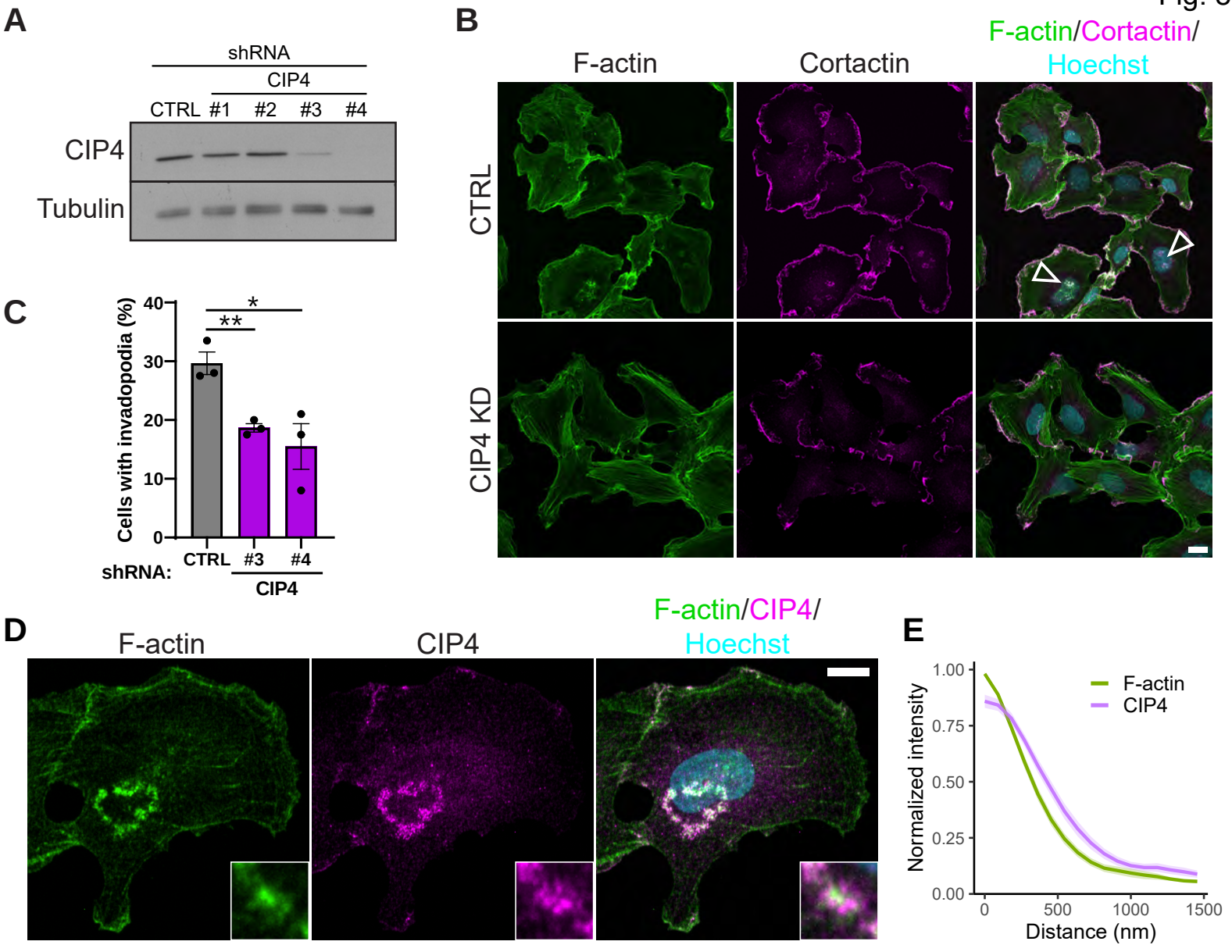
A
shRNA
CIP4
CTRL #1 #2 #3 #4
CIP4
Tubulin
B
F-actin
Cortactin
F-actin/Cortactin/
Hoechst
CTRL
CIP4 KD
C
Cells with invadopodia (%)
40
30
20
10
0
*
**
CTRL #3 #4
shRNA:
CIP4
D
F-actin
CIP4
F-actin/CIP4/
Hoechst
E
Normalized intensity
1.00
0.75
0.50
0.25
0.00
F-actin
CIP4
0 500 1000 1500
Distance (nm)

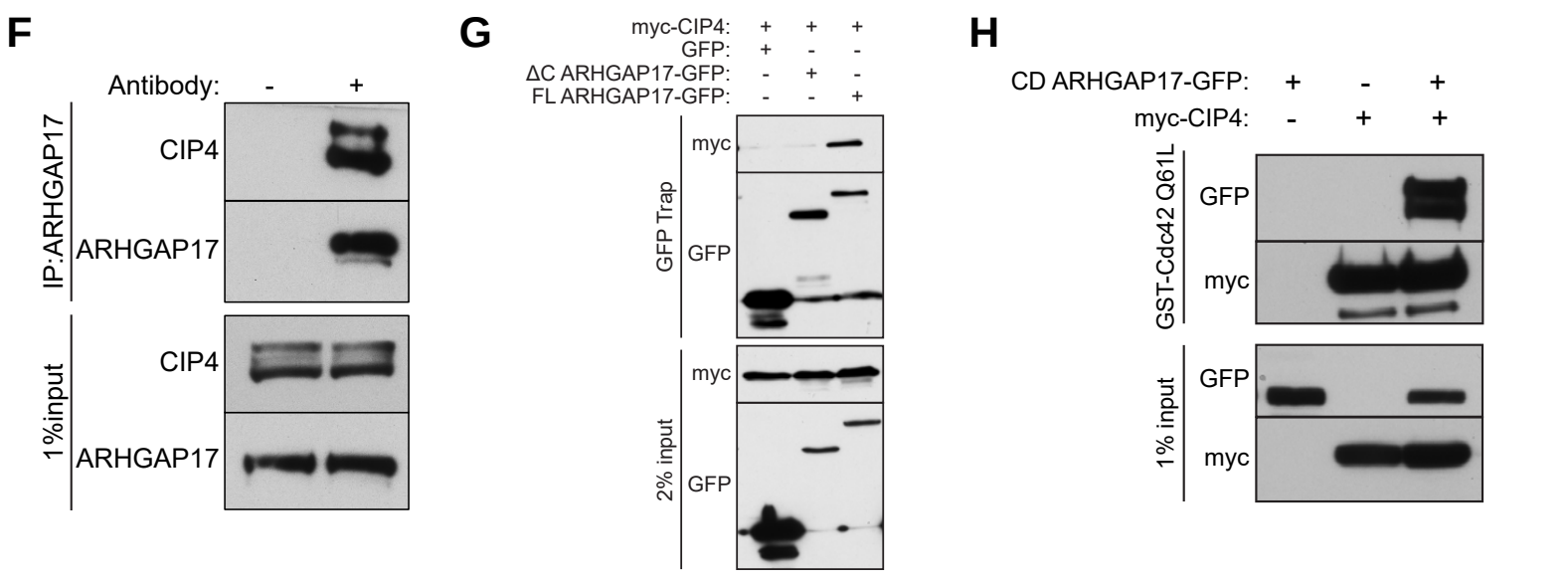
F
Antibody: - +
IP:ARHGAP17
CIP4
ARHGAP17
1%input
CIP4
ARHGAP17
G
myc-CIP4: + + +
GFP: + - -
ΔC ARHGAP17-GFP: - + -
FL ARHGAP17-GFP: - - +
GFP Trap
myc
GFP
2% input
myc
GFP
H
CD ARHGAP17-GFP: + - +
myc-CIP4: - + +
GST-Cdc42 Q61L
GFP
myc
1% input
GFP
myc

Fig. 9

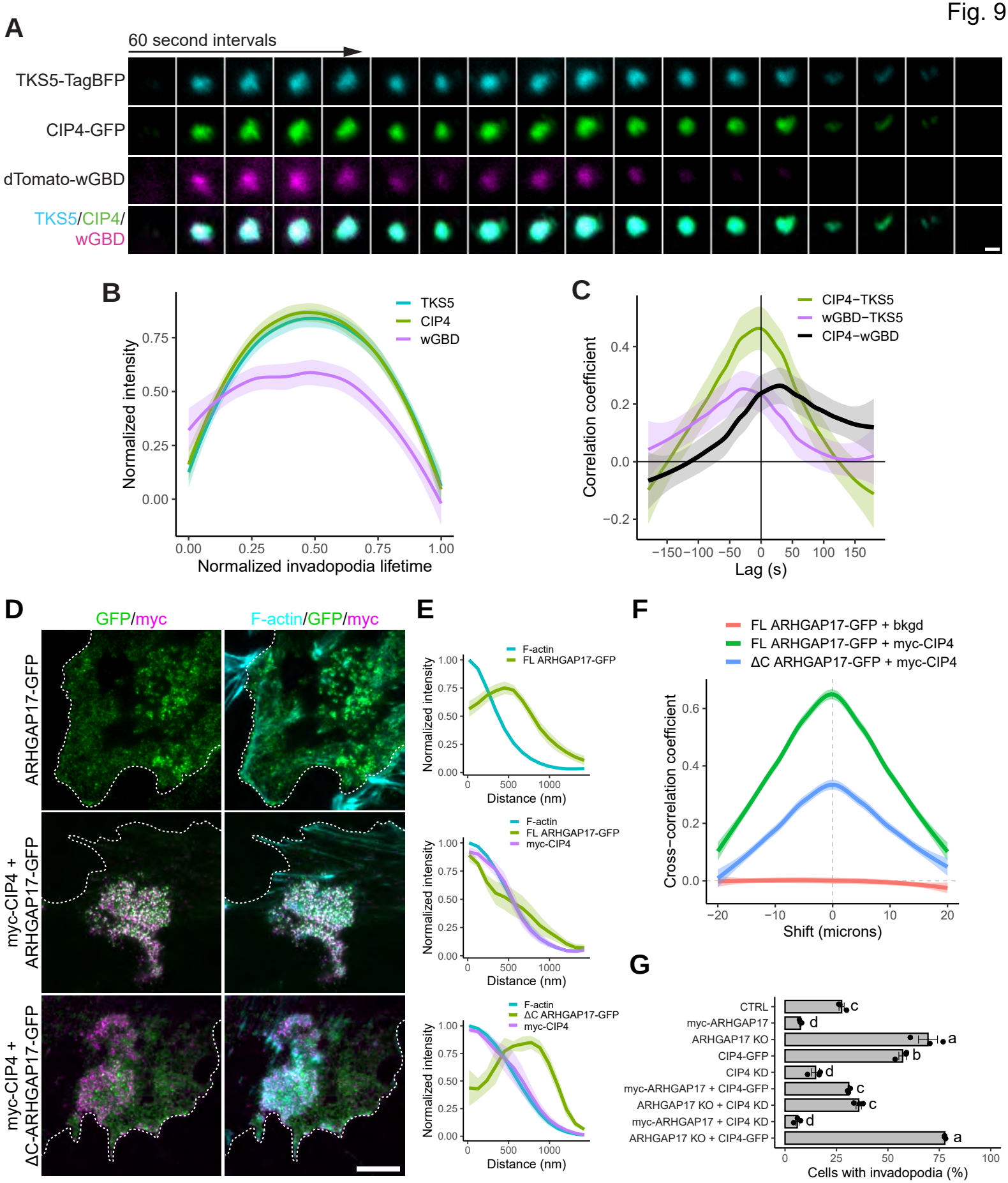
A
60 second intervals
TKS5-TagBFP
CIP4-GFP
dTomato-wGBD
TKS5/CIP4/
wGBD
B
TKS5
CIP4
wGBD
Normalized intensity
Normalized invadopodia lifetime
C
CIP4−TKS5
wGBD−TKS5
CIP4−wGBD
Correlation coefficient
Lag (s)
D
GFP/myc
F-actin/GFP/myc
ARHGAP17-GFP
myc-CIP4 +
ARHGAP17-GFP
myc-CIP4 +
ΔC-ARHGAP17-GFP
E
F-actin
FL ARHGAP17-GFP
myc-CIP4
ΔC ARHGAP17-GFP
Normalized intensity
Distance (nm)
F
FL ARHGAP17-GFP + bkgd
FL ARHGAP17-GFP + myc-CIP4
ΔC ARHGAP17-GFP + myc-CIP4
Cross−correlation coefficient
Shift (microns)
G
CTRL
myc-ARHGAP17
ARHGAP17 KO
CIP4-GFP
CIP4 KD
myc-ARHGAP17 + CIP4-GFP
ARHGAP17 KO + CIP4 KD
myc-ARHGAP17 + CIP4 KD
ARHGAP17 KO + CIP4-GFP
Cells with invadopodia (%)

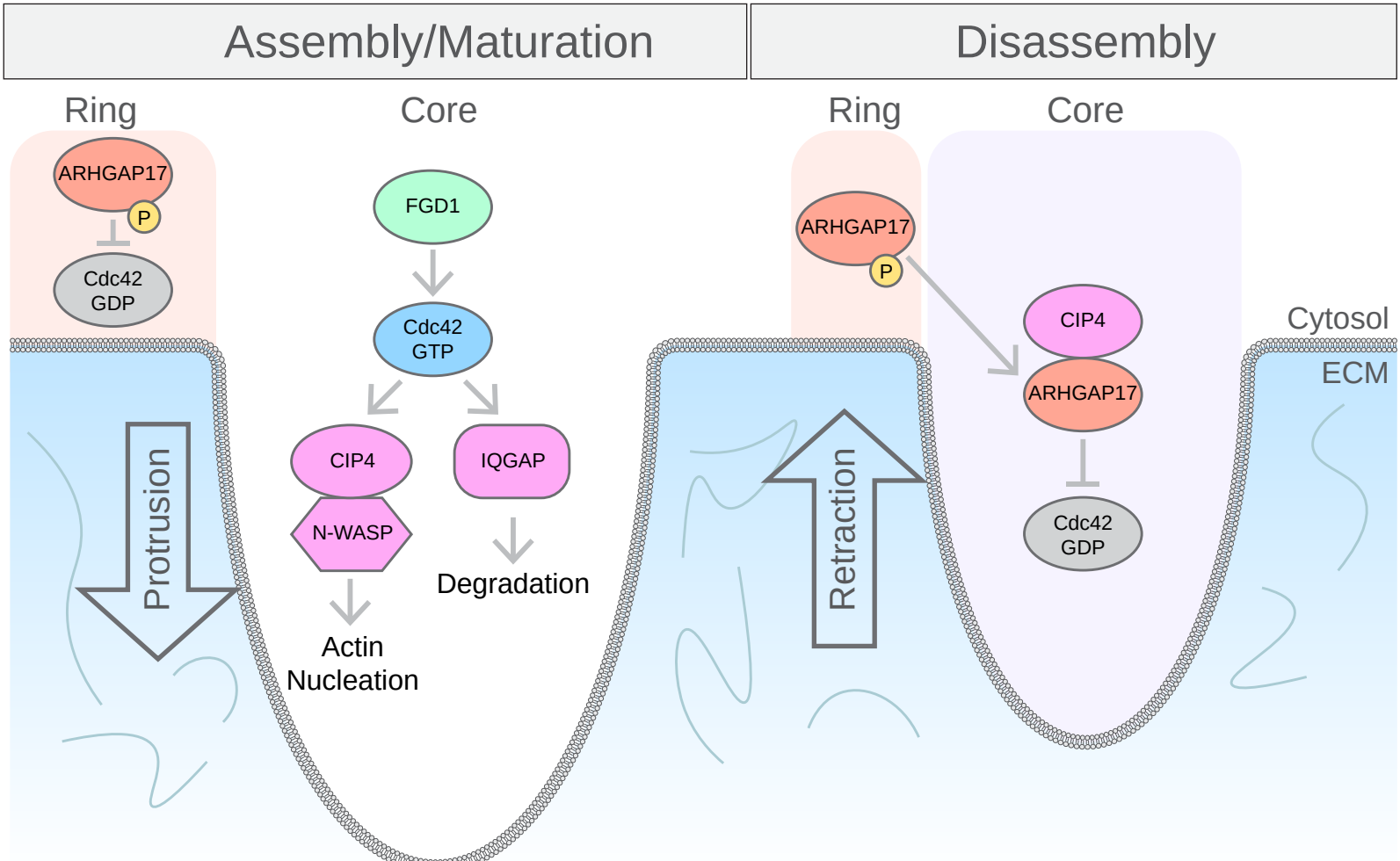
Assembly/Maturation
Disassembly
Ring
Core
Ring
Core
ARHGAP17
P
Cdc42
GDP
FGD1
Cdc42
GTP
CIP4
N-WASP
IQGAP
Degradation
Actin
Nucleation
Protrusion
ARHGAP17
P
CIP4
ARHGAP17
Cdc42
GDP
Retraction
Cytosol
ECM